Title
The Hippo pathway noncanonically drives autophagy and cell survival in response to energy stress

Journal
Molecular Cell, 83(17)

ISSN
1097-2765

Authors
Seo, Gayoung
Yu, Clinton
Han, Han
et al.

Publication Date
2023-09-01

DOI
10.1016/j.molcel.2023.07.019

Peer reviewed

HHS Public Access

Author manuscript

Mol Cell. Author manuscript; available in PMC 2024 September 07.

Published in final edited form as:

Mol Cell. 2023 September 07; 83(17): 3155–3170.e8. doi:10.1016/j.molcel.2023.07.019.

The Hippo pathway noncanonically drives autophagy and cell survival in response to energy stress

Gayoung Seo[1], **Clinton Yu**[2], **Han Han**[1], **Li Xing**[3], **Rebecca Elizabeth Kattan**[1], **Jeongmin An**[1], **Amrutha Kizhedathu**[1], **Bing Yang**[1], **Annabella Luo**[1], **Abigail L. Buckle**[1], **Delia Tifrea**[4], **Robert Edwards**[4], **Lan Huang**[2], **Huai-Qiang Ju**[5,*], **Wenqi Wang**[1,6,*]

[1]Department of Developmental and Cell Biology, University of California, Irvine, Irvine, CA 92697, USA

[2]Department of Physiology and Biophysics, University of California, Irvine, Irvine, CA 92697, USA

[3]Irvine Materials Research Institute, University of California, Irvine, Irvine, CA 92697, USA

[4]Department of Pathology, University of California Irvine, Irvine, CA 92697, USA

[5]State Key Laboratory of Oncology in South China, Sun Yat-sen University Cancer Center, Guangzhou 510060, China

[6]Lead Contact

Summary

The Hippo pathway is known for its crucial involvement in development, regeneration, organ size control, and cancer. While energy stress is known to activate the Hippo pathway and inhibit its effector YAP, the precise role of the Hippo pathway in energy stress response remains unclear. Here, we report a YAP-independent function of the Hippo pathway in facilitating autophagy and cell survival in response to energy stress, a process mediated by its upstream components MAP4K2 and STRIPAK. Mechanistically, energy stress disrupts the MAP4K2-STRIPAK association, leading to the activation of MAP4K2. Subsequently, MAP4K2 phosphorylates ATG8-family member LC3, thereby facilitating autophagic flux. MAP4K2 is highly expressed in head and neck cancer and its mediated autophagy is required for head and neck tumor growth in mice. Taken together, our study unveils a noncanonical role of the Hippo

*Correspondence: juhq@sysucc.org.cn (H.Q.J.) and wenqiw6@uci.edu (W.W.).

Author contributions

W.W. conceived and supervised the study; G.S. performed all the experiments with the assistance from H.H., R.E.K, J.A., A.K., B.Y., A.L. and A.L.B.; C.Y. and L.H. performed mass spectrometry analysis of the LC3A phosphorylation site; L.X. performed the electron microscopy analysis; D.T. and R.E. helped with the orthotopic xenograft study; H.Q.J. performed the PDX study; G.S. and W.W. wrote the manuscript.

Inclusion and diversity

We support inclusive, diverse, and equitable conduct of research.

Declaration of interests

The authors declare no competing financial interests.

pathway in energy stress response, shedding light on this key growth-related pathway in tissue homeostasis and cancer.

eTOC Blurb

Seo et al. report a YAP-independent role of the Hippo pathway in driving autophagy upon energy stress, a process mediated by its components MAP4K2 and STRIPAK. Energy stress feeds into STRIPAK to activate MAP4K2, which in turn phosphorylates LC3A to promote autophagy, cell survival, and head and neck cancer development.

Graphical Abstract

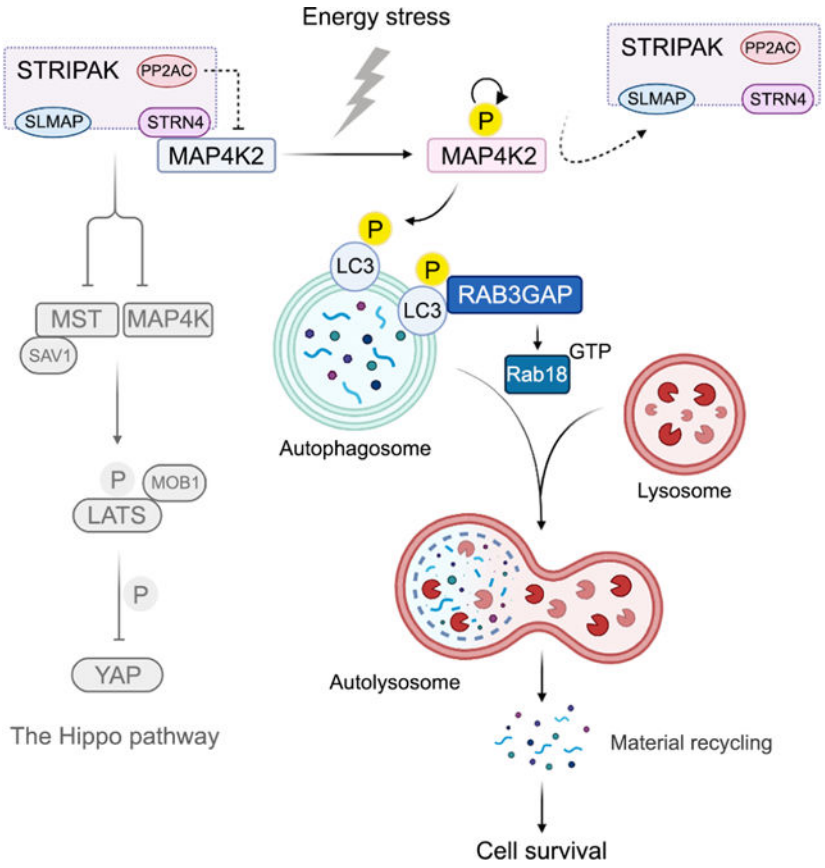

Keywords

The Hippo pathway; energy stress; MAP4K2; LC3; autophagy; STRIPAK; head and neck cancer

Introduction

The Hippo pathway is a critical regulator of development, regeneration, tissue homeostasis, and organ size, whose dysregulation has been implicated in human diseases, particularly cancer[1–4]. This pathway is regulated by a wide range of signaling events, such as growth factors, energy homeostasis, mechanical cues; however, exactly how the Hippo pathway

transduces these upstream signaling events to effects on cell proliferation and survival is still largely unknown.

The mammalian Hippo pathway is composed of a core kinase cascade comprising two Ser/Thr kinases MST1/2 and LATS1/2 with their adaptor proteins SAV1 and MOB1, respectively, downstream effector proteins YAP and TAZ, and nuclear transcription factors TEAD1–4. Upon Hippo activation, MST1/2 phosphorylate and activate LATS1/2, which in turn phosphorylate YAP/TAZ, resulting in their cytoplasmic retention and degradation. As transcriptional co-activators, un-phosphorylated YAP/TAZ are translocated into the nucleus, where they bind TEAD1–4 to promote the transcription of genes involved in numerous growth-related events. Recent studies in *Drosophila* and mammals have highlighted MAP4K-family kinases (MAP4Ks) and the striatin-interacting phosphatase and kinase (STRIPAK) complex as additional components of the Hippo pathway. MAP4Ks act in parallel to MST1/2 to phosphorylate and activate LATS1/2[5–9], while STRIPAK, a member of the protein phosphatase 2A (PP2A) family, binds and inhibits MST1/2 and MAP4Ks through its components SLMAP[10] and STRN4[11], respectively.

Among the Hippo-associated signaling contexts, we are interested in the functional interplay between the glucose-dependent energy homeostasis and the Hippo pathway discovered by us and others a few years ago[12–15]. Specifically, under glucose-rich condition, YAP is translocated into the nucleus to drive the transcription of genes involved in glucose metabolism[13,16]; under glucose starvation or energy stress conditions, activated Hippo pathway induces YAP phosphorylation at S127 to inhibit its nuclear localization, while AMPK, the master kinase in energy stress response[17], phosphorylates YAP at S94 to disrupt its association with TEAD1–4[13,14]. Notably, regardless of YAP cellular localization, the AMPK-mediated YAP phosphorylation directly targets the YAP-TEAD complex formation to inhibit YAP downstream outputs, making the Hippo-induced YAP cytoplasmic retention dispensable. This enigma indicates that the Hippo pathway could play a YAP-independent role in energy stress response.

In this study, we discovered a YAP-independent role of the Hippo pathway in facilitating autophagy and cell survival in response to energy stress. We show that MAP4K2 was required for autophagy both *in vitro* and *in vivo* and specifically protected cells against energy stress. Mechanistically, glucose starvation disrupted the association of MAP4K2 with the STRIPAK complex component STRN4 to activate MAP4K2, which in turn phosphorylated autophagy protein LC3A at S87 to drive autophagosome-lysosome fusion in autophagic flux. Moreover, MAP4K2 was highly expressed in head and neck cancer and targeting MAP4K2-mediated autophagy inhibited head and neck tumor growth. Collectively, our study not only reveals a noncanonical role of the Hippo pathway in energy stress response, but also provides insights into this key signaling pathway in growth control, stress response and cancer.

Results

MAP4K2 binds ATG8 family of autophagy proteins

To reveal additional roles of the Hippo pathway in energy stress response, we searched the published Hippo pathway interactome data[11,18–20] for preys with known functions in stress response (Table S1). Interestingly, gene ontology (GO) analysis connected the Hippo pathway protein-protein interaction network with macroautophagy (hereafter referred to as autophagy) (Figure S1A), a lysosome-dependent degradative pathway breaking down macromolecules for essential cellular processes and cell survival under stress conditions[21–23]. Among the Hippo-interacting proteins associated with autophagy were three of ATG8-family proteins (i.e., GABARAP, GABARAPL1 and GABARAPL2) (Figure S1A), which were also involved in cellular response to stimuli including starvation, nitrogen levels, nutrient levels based on an independent biological process analysis of the Hippo pathway interactome data (Figures S1B and S1C).

These ATG8-family proteins were identified as MAP4K2-interacting proteins via tandem affinity purification coupled with mass spectrometry (TAP-MS) analysis (Table S1 and Figure 1A). Additionally, MAP4K2 was reciprocally uncovered in the LC3A-, LC3B-, GABARAPL1- and GABARAPL2-associated protein complexes (Figure 1A). Indeed, *in vitro* pulldown assay showed that MAP4K2 directly bound LC3 and GABARAP proteins but not other ubiquitin-like proteins (Figure 1B). MAP4K2 was the only MAP4K-family member that strongly interacted with LC3A (Figure 1C) and GABARAP (Figure S1D). We uncovered a LC3-interacting region (LIR) motif in the MAP4K2 linker region (Figure 1D) and demonstrated that this LIR motif was required for the interaction between MAP4K2 and LC3A (Figure 1E). MAP4K2, but not its LIR motif-deletion mutant, was localized to punctate structures in the cells, which were co-localized with LC3A under control and chloroquine-treated conditions (Figure 1F) as well as nutrient-deprived conditions (Figure S1E). Loss of the LIR motif did not affect the ability of MAP4K2 to phosphorylate LATS1 hydrophobic motif (HM)-containing region C3 at T1079[24] (Figure S1F). Taken together, these data demonstrate ATG8-family proteins as *bona-fide* binding proteins for Hippo kinase MAP4K2.

MAP4K2 is required for autophagy and cell survival under energy stress conditions

We generated the MAP4K2 knockout (KO) cells using CRISPR/Cas9 (Figure 2A) and found that loss of MAP4K2 increased the expression of autophagy proteins LC3 and p62 (Figure 2A) but did not affect YAP S127 phosphorylation (Figure 2A) or its cellular localization (Figures S2A and S2B). Moreover, MAP4K2 deficiency increased LC3A puncta even under normal culture condition (Figures 2B and 2C). Electron microscopy revealed the accumulated vesicle-like structures in the MAP4K2 KO cells, resembling the ones observed in the chloroquine-treated cells (Figure 2D). We also confirmed these findings using a MAP4K2 inhibitor, TL4–12, which can target the ability of MAP4K2 to rescue YAP cytoplasmic localization in the MST/MAP4K-8KO cells (Figures S2C and 2E). Consistently, TL4–12-treated cells showed elevated expression of LC3 and p62 (Figure 2F) but no change in YAP S127 phosphorylation (Figure 2F) or its cellular localization (Figures S2D and S2E). TL4–12 treatment also induced the formation of LC3A puncta in different cells under

normal culture condition (Figures 2G, 2H and S2F) and lipid droplet accumulation in the livers of fasted mice (Figures 2I and 2J). Together with the facts that inhibiting either the class III PI3K complex (Figures S2G and S2H) or LC3A lipidation (Figures S2I and S2J) reduced the accumulated LC3A puncta in the MAP4K2 KO cells, these data show a YAP-independent role of MAP4K2 in regulating autophagy.

Since autophagy protects cells against various stresses, we next examined whether MAP4K2 could regulate cell survival under stress conditions. Interestingly, loss of MAP4K2 dramatically reduced cell viability upon glucose starvation and HBSS treatment but did not affect cells when cultured under serum starvation and amino acids starvation (Figures 2K and 2L). Targeting MAP4K2 activity by TL4–12 also significantly reduced the cell viability under glucose starvation and HBSS treatment (Figures 2M and 2N). Collectively, these results suggest that MAP4K2 is required for cell survival in energy stress response.

MAP4K2 drives autophagy by phosphorylating LC3A at S87

Regarding the mechanism, we found that reconstituting wild-type MAP4K2, but not its kinase dead mutant (K45R) or LIR motif-deletion mutant (ΔLIR), reversed the accumulated LC3A puncta in the MAP4K2 KO cells under both normal culture condition (Figures S3A, 3A and 3B) and glucose starvation (Figures S3A–S3C). Moreover, our *in vitro* kinase assay showed that MAP4K2, but not its kinase dead mutant (K45R), induced LC3A phosphorylation as indicated by the higher band shift in phos-tag gel (Figure 3C). Mass spectrometry analysis further revealed S87 as the MAP4K2 phosphorylation site on LC3A (Figure 3D). This finding was confirmed using MAP4K2 *in vitro* kinase assay where the S87A mutation largely reduced the band shift of GST-LC3A in phos-tag gel (Figure 3E) as well as a phospho-antibody against p-LC3A S87 both *in vitro* (Figure 3F) and *in vivo* (Figure 3G). Loss of MAP4K2 dramatically reduced LC3A S87 phosphorylation (Figure 3G). These data together demonstrate that MAP4K2 phosphorylates LC3A at S87.

The LC3A S87 site and its nearby amino acid sequence are conserved among all the LC3 proteins in mammals and amphibians (Figure 3H). The MAP4K2 LIR motif can be traced to fish but not its fly orthologous protein *Happyhour* (Figure 1D). These findings thus raise an interesting possibility that the MAP4K2-mediated LC3 regulation co-evolved with vertebrate species.

We next examined the role of LC3A S87 phosphorylation in MAP4K2-dependent autophagy and cell survival. Interestingly, the S87A mutation largely induced the number of LC3A puncta under both control (Figures 3I and 3J) and glucose starvation (Figures S3D and S3E) conditions, which resembled the phenotypes observed in the MAP4K2 KO cells (Figures 2B, 2C, S2G and S2H). Expressing LC3A S87 phosphomimic mutant (S87D), but not its S87A mutant, significantly rescued MAP4K2 KO cell viability under glucose starvation condition (Figures 3K and 3L). These data show that MAP4K2 drives autophagy and cell survival by phosphorylating LC3A at S87.

Notably, there was still a significant band shift of LC3A S87A mutant in phos-tag gel (Figure 3E), suggesting that MAP4K2 may phosphorylate additional sites of LC3A. We then mutated each remaining Ser/Thr site on LC3A S87A mutant (Figure S3F) for *in vitro*

kinase assay and eventually revealed S12 and S115 as additional MAP4K2 phosphorylation sites on LC3A (Figures S3G and S3H). As for other ATG8-family proteins, MAP4K2 induced a significant band shift of LC3B, LC3C and GABARAP in phos-tag gel (Figure S3I). Mutating the conserved LC3A S87 site on LC3B (i.e., S87) and LC3C (i.e., S93) (Figure S3J) largely but not completely reduced their band shift in phos-tag gel (Figure S3K), suggesting that MAP4K2 could phosphorylate other sites on LC3B and LC3C. In line with this notion, LC3A S12 and S115 sites are also conserved on LC3B and LC3C (Figure S3J). In contrast, none of these identified LC3A phosphorylation sites was conserved on GABARAP (Figure S3J). Mutating GABARAP T87, one potential phosphorylation site localized in the region nearby the conserved LC3A S87 site, showed only mild effect on the MAP4K2-induced GABARAP band shift in phos-tag gel (Figure S3K), suggesting that MAP4K2 may phosphorylate GABARAP at different sites. Despite these facts, given the critical role of LC3A S87 phosphorylation in MAP4K2-mediated autophagy (Figures 3I–3L, S3D and S3E), we majorly focused on the MAP4K2-induced LC3A S87 phosphorylation in this study.

MAP4K2-mediated LC3A S87 phosphorylation is required for autophagosome-lysosome fusion in autophagic flux

Notably, inhibition of MAP4K2 increased both LC3-I and LC3-II (Figures 2A and 2F) but did not affect the activation or expression of key autophagy components/regulators like ULK1, AMPK, mTOR and ATG5 (Figure 4A). The accumulated LC3A puncta in the MAP4K2 KO cells were partially co-localized with early autophagosome marker ATG16L1[25,26] but displayed extensive co-localization with late autophagosome marker STX17[27] (Figures 4B and S4A). We hardly detected the co-localization between the accumulated LC3A puncta and lysosome marker LAMP1 in the MAP4K2 KO cells (Figures 4B and S4A). These data together suggest that MAP4K2 acts in the late stage of autophagy.

To determine whether late autophagosomes would be able to fuse with lysosomes in the MAP4K2 KO cells, we generated a tandem monomeric mCherry-GFP-LC3A construct to measure the autophagosome-lysosome fusion[28,29]. Autophagosomes that have not fused with lysosomes exhibit both GFP and mCherry signals, while after fusion they only show mCherry signal, because the GFP signal is sensitive to the acidic condition in the lysosome lumen. Glucose starvation and HBSS treatment induced autophagosome-lysosome fusion in wild-type cells (i.e., mCherry signal only – red) (Figures 4C and 4D). In contrast, such autophagosome-lysosome fusion was abolished in the MAP4K2 KO cells (Figures 4C and 4D) and MAP4K2 inhibitor TL4–12-treated cells (Figures 4E and 4F) (i.e., both GFP and mCherry signals – yellow). As a control, the autophagosome-lysosome fusion inhibitor chloroquine largely induced “yellow” LC3A puncta in both wild-type and MAP4K2 KO HEK293A cells (Figures 4C and 4D). Interestingly, the mCherry-GFP-LC3A S87A puncta mostly showed “yellow” color upon glucose starvation and HBSS treatment, while its S87D mutant puncta displayed “red” color (Figures 4G and 4H). Furthermore, expression of LC3A S87D mutant but not its S87A mutant largely rescued the autophagosome-lysosome fusion in the MAP4K2 KO cells and TL4-12-treated cells (Figures S4B and S4C). Collectively, these results show that MAP4K2 facilitates autophagosome-lysosome fusion by phosphorylating LC3A at S87.

Since LC3A S87 site is conserved on LC3B and LC3C (Figure S3J), we examined such regulation for LC3B and LC3C. Indeed, the S87A mutation increased the number of LC3B puncta (Figures S3L and S3M) and interfered with its autophagosome-lysosome fusion (Figures S3N and S3O). Given the large number of LC3C puncta observed in cells, we did not observe a significant increase of LC3C S93A mutant puncta (Figures 3L and S3M). However, the S93A mutation was able to inhibit the LC3C autophagosome-lysosome fusion (Figures S3N and S3O). These data suggest a similar regulation of LC3 proteins in autophagic flux by MAP4K2.

LC3A S87 phosphorylation induces autophagosome-lysosome fusion through the RAB3GAP1/2-Rab18 pathway

It is known that LC3 drives autophagosome-lysosome fusion by recruiting PLEKHM1 to induce the recognition/fusion between autophagosomes and lysosomes[30,31]. LC3 also counteracts the FYCO1-mediated kinesin-driven autophagosome movement towards the cell periphery, thereby spatially moving autophagosomes to lysosomes[31–33]. Different from the previous study[30], we failed to detect the interaction between LC3A and PLEKHM1 (Figure S4D). LC3A S87A mutant showed reduced interaction with FYCO1 as compared to LC3A and its S87D mutant (Figures S4E and S4F). Given the negative role of FYCO1 in autophagosome-lysosome fusion[31–33], reducing the interaction between FYCO1 and LC3A should have promoted the autophagosome-lysosome fusion; however, this was not the case based on our data (Figures 4G, 4H, S4B and S4C). These results indicate that LC3A S87 phosphorylation mediates autophagosome-lysosome fusion through a yet-to-be identified mechanism.

To address it, we performed a comparative proteomic analysis for the LC3A- and its S87A mutant-associated proteins complexes under glucose starvation condition and identified a group of high confident interacting proteins (i.e., SAINT score ≥ 0.8) showing significant binding difference between LC3A and its S87A mutant (Figure 5A). Among them, two Warburg Micro and Martsolf Syndrome-associated proteins RAB3GAP1 and RAB3GAP2[34–36] were revealed as LC3A-binding proteins, whose interaction with LC3A was suppressed by its S87A mutation (Figure 5A). Our pulldown experiments confirmed the interaction between LC3A and RAB3GAP1/2 (Figure 5B) and showed that either the S87A mutation (Figure 5C) or loss of MAP4K2 (Figure 5D) inhibited the binding of LC3A with RAB3GAP1. As controls, the S87A and S87D mutations did not affect the association of LC3A with the known LC3-binding proteins p62 (Figure S4G) or NDP52 (Figure S4H). As for other tested autophagy proteins like FIP200 (Figure S4I) and NBR1 (Figure S4J), we hardly detected their interactions with LC3A or its S87A/D mutants.

Glucose starvation and chloroquine treatment significantly promoted the co-localization of RAB3GAP1 with LC3A but not its S87A mutant (Figures 5E and 5G). Loss of MAP4K2 diminished the localization of RAB3GAP1 to LC3A puncta even under chloroquine-treated condition but did not affect the co-localization between RAB3GAP1 and LC3A S87D mutant (Figures 5F and 5G). The RAB3GAP1/2 complex is known to promote autophagosome-lysosome fusion by activating Rab18 and its downstream effectors like Vps34 and Rab7[37–40]. To further assess the role of the RAB3GAP1/2 complex in MAP4K2/

LC3A-induced autophagosome-lysosome fusion, we examined Rab18 in this process. As shown in Figures 5H and 5I, expression of Rab18 constitutively active mutant (Q67L), but not its inactive mutant (S22N), largely rescued the mCherry-GFP-LC3A-indicated autophagosome-lysosome fusion in the HBSS-treated MAP4K2 KO cells. Additionally, expression of Rab18 Q67L mutant rescued the autophagosome-lysosome fusion of mCherry-GFP-LC3A S87A mutant in the HBSS-treated HEK293A cells, while expressing its S22N inactive mutant failed to do so (Figures 5J and 5K). Furthermore, expressing Rab18 Q67L mutant but not its S22N mutant significantly rescued MAP4K2 KO cell viability under glucose starvation condition (Figures S4K and S4L).

Collectively, these results suggest that MAP4K2-mediated LC3A S87 phosphorylation acts through the RAB3GAP1/2-Rab18 pathway to drive autophagosome-lysosome fusion.

MAP4K2 is autophosphorylated at S170 for activation

To determine the regulation of MAP4K2 under stress conditions, we predicted that MAP4K2 could be modulated by autophosphorylation, because MAP4K2 belongs to STE20-like kinase family and some of this kinase family members like MST1/2 are known to activate themselves via autophosphorylation[41–45]. By taking MST1/2 as controls, we identified S170 as a potential autophosphorylation site for MAP4K2, which is localized in the kinase domain of MAP4K2 and conserved in different species including its *Drosophila* ortholog *Happyhour* (*Hppy*) (Figure 6A). Indeed, MAP4K2 can homodimerize (Figure 6B). MAP4K2 kinase dead mutation (K45R) significantly inhibited its S170 phosphorylation (Figure 6C). MAP4K2 S170 phosphorylation was also largely reduced upon TL4–12 treatment (Figure 6D). Expressing wild-type MAP4K2 induced the phosphorylation of its kinase dead mutant (K45R) at S170 in the MST/MAP4K-8KO cells (Figure 6E). Interestingly, the S170A mutation inhibited the abilities of MAP4K2 to phosphorylate LATS1 at T1079 (Figure S1F), to rescue YAP cytoplasmic translocation in the MST/MAP4K-8KO cells (Figure S5A), to phosphorylate LC3A *in vitro* (Figure 6F), and to reduce the number of LC3A puncta in the MAP4K2 KO cells (Figures 6G and 6H). Loss of the LIR motif did not affect MAP4K2 S170 phosphorylation (Figure S5B). These findings together demonstrate that MAP4K2 is autophosphorylated at S170, which is required for its activation.

Glucose starvation activates MAP4K2 by targeting its binding with STRIPAK^{STRN4}

Among the tested stress conditions, glucose starvation and HBSS treatment significantly increased MAP4K2 S170 phosphorylation (Figure 6I), while serum starvation (Figure 6J) and amino acids starvation (Figure 6K) failed to do so. Consistently, glucose starvation increased LC3A S87 phosphorylation (Figure 6L and S5C), while this was not the case for other tested stress conditions like serum starvation (Figure S5D) or amino acids starvation (Figure S5E). Together with the previous findings (Figures 2K–2N), these results suggest a unique role of MAP4K2 in driving autophagy in response to energy stress.

Since MAP4Ks are negatively regulated by the STRIPAK complex via its component STRN4[11], we examined whether STRIPAK^{STRN4} was involved in energy stress-induced MAP4K2 activation. Indeed, depleting STRN4 largely increased the phosphorylation of

MAP4K2 at S170 (Figure 6M), while overexpressing STRN4 inhibited it (Figure S5F). Furthermore, glucose starvation failed to further enhance MAP4K2 S170 phosphorylation in the STRN4 KO cells (Figure 6N), suggesting a critical role of STRIPAK^{STRN4} in control of MAP4K2 activation by energy stress. We did not observe a significant change of the STRIPAK complex formation upon glucose starvation (Figure S5G) but found that the interaction between STRN4 and MAP4K2 was largely reduced under glucose starvation condition (Figure 6O). As controls, serum starvation and amino acids starvation did not affect the association of MAP4K2 with STRN4 (Figures 6P and 6Q). Taken together, these results show that energy stress activates MAP4K2 by reducing its binding with the STRIPAK^{STRN4} complex.

MAP4K2 is highly expressed in head and neck cancer

Cancer cells are able to survive when exposed to stress conditions by using autophagy to meet their high metabolic and energetic demands of proliferation[46–49]. Given the critical role of MAP4K2 in driving autophagy, we examined MAP4K2 in human cancer.

Interestingly, *MAP4K2* was highly expressed in head and neck cancer (HNC) as compared to normal tissue (Figure 7A). Elevated *MAP4K2* was correlated with poor overall survival rate for HNC patients (Figure 7B). We also detected a high level of MAP4K2 in the tested HNC cells as compared to a normal mammary epithelial cell line MCF10A (Figure 7C). We failed to obtain the MAP4K2 KO HNC cells, thus turned to using shRNAs to knockdown MAP4K2 in the HNC cells (Figure S6A). Consistent with the findings observed in HEK293A cells, MAP4K2 shRNA-transduced HNC cells showed increased LC3 expression (Figure S6A), accumulated LC3A puncta (Figure S6B), impaired autophagosome-lysosome fusion (Figures S6C and S6D), and reduced cell viability under glucose starvation condition (Figures S6E–S6H). MAP4K2 inhibitor TL4–12 treatment also increased LC3A puncta in the HNC cells (Figure S6B). Downregulation of MAP4K2 diminished LC3A S87 phosphorylation in the HNC cells (Figure S6I). Expressing LC3A S87D mutant but not its S87A mutant significantly rescued the MAP4K2 shRNA-transduced HNC cell viability under glucose starvation condition (Figures S6J–S6O). These results consistently show a critical role of MAP4K2 in regulating autophagy in HNC cells. We further examined the expression of MAP4K2 in HNC patient samples and found that MAP4K2 was highly expressed in multiple types of head and neck carcinomas, such as the tumors in larynx (84%) and tongue (100%) (Figures 7D, S7A and S7B). The LC3A and its S87 phosphorylation levels were also elevated in these HNC patient samples (Figures 7D, S7A and S7B). These data together indicate a potentially oncogenic role of MAP4K2 in HNC development.

MAP4K2-mediated autophagy is required for head and neck cancer development

To test this hypothesis, we chose a tongue-derived HNC cell line CAL-27 for an orthotopic xenograft study. Indeed, loss of MAP4K2 dramatically suppressed the CAL-27 tumor growth in mouse tongue tissues (Figures S7C, 7E and 7F). Reconstitution of LC3A S87D mutant, but not its S87A mutant, largely rescued MAP4K2-deficient CAL-27 xenograft tumor growth in mouse tongues (Figures S7D–S7F). In addition, TL4–12 treatment significantly inhibited the CAL-27 xenograft tumor growth in mouse tongues (Figures S7G

and S7H), while expressing LC3A S87D mutant but not its S87A mutant largely attenuated the TL4–12-induced inhibitory effect on the tumor growth (Figures S7G and S7H). These results demonstrate an oncogenic role of MAP4K2 in HNC development by facilitating autophagy.

To further verify our findings in a model resembling the clinical setting, we assessed the antitumor effect of TL4–12 using the patient-derived xenograft (PDX) models developed from the tumors of two HNC patients. Indeed, TL4–12 treatment significantly inhibited PDX tumor size and weight (Figures S7I and 7G–7I) but had no or mild effect on the mouse body weight (Figure 7J). These data suggest MAP4K2 inhibitor TL4–12 as an effective therapeutic agent for head and neck cancer.

Discussion

Autophagy can be triggered by various stresses, whereas the MAP4K2-mediated autophagy specifically responds to energy stress as evidenced by the following facts. First, MAP4K2-deficient cells were highly sensitive to glucose starvation and HBSS treatment but not serum starvation or amino acids starvation (Figures 2K–2N). Second, expressing LC3A phosphomimic S87D mutant rescued MAP4K2 KO cell viability under energy stress conditions (Figures 3K and 3L). Third, MAP4K2 activity (Figures 6I–6K) and LC3A S87 phosphorylation (Figures 6L and S5C–S5E) were specifically induced by energy stress. Lastly, only glucose starvation but not serum starvation or amino acids starvation targeted the interaction of MAP4K2 with its upstream inhibitor STRIPAK^{STRN4} (Figures 6O–6Q). These findings pinpoint a MAP4K2-centered signaling cascade facilitating autophagy and cell survival in response to energy stress.

Our study presents a critical role of the STRIPAK complex in transducing energy stress to MAP4K2 and its downstream events. Since STRIPAK also mediates the signals of growth factors (e.g., serum, lysophosphatidic acid) to regulate the Hippo pathway[50], our findings further highlight STRIPAK as an essential Hippo component integrating upstream signaling events into the effects on the Hippo core kinase cascade. In line with this notion, discovering the role of STRIPAK in transducing energy stress to MAP4K2 could shed light on the poorly characterized mechanism underlying the glucose/energy homeostasis-dependent Hippo pathway regulation.

Although the RAB3GAP1/2-Rab18 pathway was shown to participate in the MAP4K2/LC3A-induced autophagosome-lysosome fusion (Figure 5) and cell survival (Figures S4K and S4L), we did not further characterize its downstream events involved in this process, as previous studies have provided evidence for so. The RAB3GAP1/2 complex promoted autolysosome formation by activating Rab18 to bind Vps34 complex[39]. Activated Rab18 cooperated with Rab7 to induce autophagosome maturation and its subsequent fusion with lysosome [51]. Our unpublished TAP-MS analysis of the Rab18-Q67L- and Rab18-S22N-associated protein complexes further revealed potential downstream effectors of Rab18 known involved in autophagosome-lysosome fusion, such as LAMP2[52], Rab7[51,53], NSF/SNARE[54], CAMK2A/D[55], providing additional insights into the role of the RAB3GAP1/2-Rab18 pathway in this process.

The Hippo pathway has been connected with autophagy through other mechanisms. MST1/2 activate autophagy by phosphorylating LC3B at T35[56], which antagonizes the FYCO1-dependent directional transport of autophagosome[57]. MST1 phosphorylates Beclin1 at T108 to target the Atg14L-Beclin1-Vps34 complex and inhibit autophagy[58]. MST1 also functions together with RASSF1 to initiate autophagy by restricting PI3K-AKT-mTOR pathway[59]. YAP and TAZ regulate autophagy by promoting the transcription of genes involved in autophagosome formation[60] and autophagic flux[61] in response to mechanical cues. Here, unveiling the Hippo components STRIPAK and MAP4K2 as regulators of autophagy not only underscored the crucial role of the Hippo pathway in this key survival machinery, but also enriched our understanding of the Hippo pathway in stress response, tissue homeostasis and cancer from a different perspective.

Limitations of the study

First, our current study is majorly focused on the role of MAP4K2 in facilitating autophagic flux by phosphorylating LC3A at S87; however, whether MAP4K2 exerts other functions in autophagy remains to be elucidated. For example, MAP4K2 also phosphorylates S12 and S115 on LC3A (Figures S3F–S3H). Among them, LC3A S12 is known to be phosphorylated by PKA and PKCλ/τ to induce neurite growth[62] and inhibit liver tumorigenesis[63], respectively. In addition, MAP4K2 binds and phosphorylates other ATG8-family proteins (Figures 1B and S3I), which are known to have different functions in autophagy[64]. These facts indicate a complex role of MAP4K2 in autophagy through ATG8-family proteins, which deserves further investigation.

Second, although energy stress activates MAP4K2 by diminishing its association with STRIPAK (Figures 6M–6O, S5F and S5G), the underlying mechanism remains unknown. Moreover, given the critical role of STRIPAK in restricting the MAP4Ks activities[11], it will be interesting to determine whether other MAP4K-family kinases would be similarly regulated by energy stress.

Third, in contrast to the known tumor suppressive role of the Hippo pathway in cancer, our study revealed MAP4K2 as an oncogenic kinase and a potential therapeutic target in head and neck cancer through autophagy (Figures 7 and S7). This is consistent with previous findings showing a pivotal role of autophagy in head and neck cancer development[65–67]. Since autophagy has been suggested as a therapeutic target for different types of cancers, whether MAP4K2 can be targeted for treating other autophagy-dependent cancers deserves to be further investigated.

STAR Methods

Resource Availability

Lead Contact—Further information and requests for resources and reagents should be directed to and will be fulfilled by the Lead Contact, Dr. Wenqi Wang (wenqiw6@uci.edu).

Materials Availability

Any reagents that are unique to this study will be made available upon request.

Data and Code Availability

- All original imaging data are available Mendeley data. All data are publicly available as of the date of publication. Accession numbers and DOI are listed in the key resources table.
- This paper does not report any original code.
- Any additional information required to reanalyze the data reported in this paper is available from the lead contact upon request.

Experimental Model and Study Participant Details

Cell Lines—HEK293T (a female cell line, ATCC: CRL-3216), MCF10A (a female cell line, ATCC: CRL-10317), Hep3B (a male cell line, ATCC: HB-8064), HepG2 (a male cell line, ATCC: HB-8065), MDA-MB-231 (a female cell line, ATCC: CRM-HTB-26), and HeLa (a female cell line, ATCC: CRM-CCL-2) cell lines were purchased from ATCC and kindly provided by Dr. Junjie Chen (MD Anderson Cancer Center). HEK293A (a female cell line, Thermo Fisher Scientific: R70507) cell line was kindly provided by Dr. Jae-Il Park (MD Anderson Cancer Center). FaDu (a male cell line, ATCC: HTB-43), CAL-27 (a male cell line, ATCC: CRL-2095), A-253 (a male cell line, ATCC: HTB-41), SCC-4 (a male cell line, ATCC: CRL-1624), BxPC3 (a female cell line, ATCC: CRL-1687), and PANC1 (a male cell line, ATCC: CRL-1469) cell lines were purchased from ATCC.

HEK293T, HEK293A, CAL-27, PANC1, Hep3B, HepG2, MDA-MB-231 and HeLa cells were maintained in Dulbecco's Modified Eagle's Medium (DMEM) supplemented with 10% fetal bovine serum at 37 °C in 5% CO_2 (v/v). MCF10A cells were maintained in DMEM/F12 medium supplemented with 5% horse serum, 200 ng/mL epidermal growth factor, 500 ng/mL hydrocortisone, 100 ng/mL cholera toxin and 10 μg/mL insulin at 37 °C in 5% CO_2 (v/v). FaDu cells were maintained in minimum essential medium (MEM) supplemented with 10% fetal bovine serum at 37 °C in 5% CO_2 (v/v). A-253 cells were grown in McCoy's 5A medium with 10 % fetal bovine serum at 37 °C in 5% CO_2 (v/v). SCC-4 cells were cultured in DMEM/F12 medium supplemented with 10% fetal bovine serum and 400 ng/mL hydrocortisone at 37 °C in 5% CO_2 (v/v). BxPC3 cells were cultured in RPMI-1640 medium supplemented with 10% fetal bovine serum at 37 °C in 5% CO_2 (v/v). All the culture media contain 1% penicillin and streptomycin.

Animals—The lipid droplet study was followed institutional guidelines, approved by the Institutional Animal Care and Use Committee (IACUC; protocol number AUP-19-112) of the University of California, Irvine, and performed under veterinary supervision. Four-week-old female C57BL/6 mice were purchased from Jackson Laboratory and used for the liver lipid droplet study.

The orthotopic xenograft tumor experiments were followed institutional guidelines, approved by the Institutional Animal Care and Use Committee (IACUC; protocol number AUP-19-112) of the University of California, Irvine, and performed under veterinary supervision. Eight-week-old female athymic nude (nu/nu) mice were purchased from Jackson Laboratory and used for the orthotopic xenograft study.

The patient-derived xenograft (PDX) tumor experiments were followed institutional guidelines, approved by the Institutional Animal Care and Use Committee (IACUC; protocol number L025501202212006) of Sun Yat-sen University Cancer Center, and performed under veterinary supervision. Six-week-old female NOD-SCID-IL2rg (NSG) mice were purchased from Biocytogen Pharmaceuticals (Beijing) and used for the PDX study.

All the mice were kept in a pathogen-free environment.

Method Details

Antibodies and Chemicals—For Western blotting, anti-Flag (M2) (F3165–5MG, 1:5000 dilution), anti-Flag (M2)-peroxidase (HRP) (A8592-1MG, 1:5000 dilution), anti-α-tubulin (T6199-200UL, 1:5000 dilution), and anti-β-actin (A5441-100UL, 1:5000 dilution) antibodies were obtained from Sigma-Aldrich. Anti-Myc (sc-40, 1:500 dilution), anti-SLMAP (sc-100957, 1:1000 dilution), and anti-MOB4 (sc-137228, 1:1000 dilution) antibodies were purchased from Santa Cruz Biotechnology. Anti-hemagglutinin (HA) antibody (MMS-101P, 1:3000 dilution) was obtained from BioLegend. Anti-STRN (A304-537A, 1:1000 dilution), anti-STRN4 (A304-573A-T, 1:1000 dilution), and anti-FAM40A/STRIP1 (A304-644A, 1:1000 dilution) antibodies were obtained from FORTIS Life Sciences. Anti-phospho-YAP (S127) (4911S, 1:1000 dilution), anti-LC3A/B (12741S, 1:500 dilution), anti-SQSTM1/p62 (88588S, 1:500 dilution), anti-GAPDH (5174S, 1:2,000 dilution), anti-phospho-ULK1 (Ser555) (5869S, 1:1000 dilution), anti-phospho-ACC (Ser79) (3661S, 1:1000 dilution), anti-phospho-p70 S6K (Thr389) (9234S, 1:500 dilution), anti-ATG5 (2630S, 1:1000 dilution), anti-PP2A C (2038S, 1:1000 dilution), anti-phospho-AKT (Ser473) (4060s, 1:1000 dilution), and anti-phospho-p44/42 MAPK (ERK1/2) (Thr202/Tyr204) (4370S, 1:2000 dilution) antibodies were purchased from Cell Signaling Technology. Anti-phospho-MAP4K2 (Ser170) antibody (AB-PK646, 1:1000 dilution) was purchased from Kinexus. Anti-phospho-LC3A (Ser87) antibody (1:500 dilution) was raised by immunizing a rabbit with keyhole limpet hemocyanin-conjugated phospho-peptide CQAFFLLVNQH(phospho-S)MVSVSTPI and affinity purified using SulfoLink peptide Coupling Resin (Thermo Fisher Scientific). Anti-MAP4K2 antibody (1:200 dilution) was raised by immunizing a rabbit with a bacterially expressed and purified MBP-MAP4K2 fusion protein containing the 293~550 amino acids of human MAP4K2. Anti-GST antibody (1:5000 dilution) was raised by immunizing a rabbit with bacterially expressed and purified full-length GST protein. Anti-CTTNBP2NL antibody (1:200 dilution) was raised by immunizing a rabbit with a bacterially expressed and purified MBP-CTTNBP2NL fusion protein containing the 571~820 amino acids of human CTTNBP2NL. Anti-YAP antibody (1:1,000 dilution) was generated as described previously[68], which was raised by immunizing a rabbit with bacterially expressed and purified GST-YAP full-length fusion protein. All the antisera were affinity-purified using AminoLink Plus Immobilization and Purification Kit (Pierce).

For immunofluorescent staining, anti-YAP antibody (sc-101199, 1:200 dilution) was purchased from Santa Cruz Biotechnology. Anti-LC3A/B antibody (12741S, 1:100 dilution) was obtained from Cell Signaling Technology. Anti-Flag (M2) (F3165-5MG, 1:2000

dilution) and anti-Flag (F7425-.2MG, 1:2000 dilution) antibodies were purchased from Sigma-Aldrich.

For immunohistochemical staining, anti-LC3A antibody (4599S, 1:200 dilution) was purchased from Cell Signaling Technology. Anti-MAP4K2 antibody (1:50 dilution) was raised by immunizing a rabbit with a bacterially expressed and purified MBP-MAP4K2 fusion protein containing the 293~550 amino acids of human MAP4K2. Anti-phospho-LC3A (Ser87) antibody (1:50 dilution) was raised by immunizing a rabbit with keyhole limpet hemocyanin-conjugated phospho-peptide CQAFFLLVNQH(phospho-S)MVSVSTPI and affinity purified using SulfoLink peptide Coupling Resin (Thermo Fisher Scientific).

TL4-12 (#5910, 10 mg) was purchased from TOCRIS.

Constructs and Viruses—Plasmids encoding the indicated genes were obtained from the Human ORFeome V5.1 library or purchased from the DNASU Plasmid Repository. All constructs were generated via polymerase chain reaction (PCR) and sub-cloned into a pDONOR201 vector using Gateway Technology (Thermo Fisher Scientific) as entry plasmids. Gateway-compatible destination vectors with the indicated SFB tag, GST tag, GFP tag, mCherry tag, HA tag, Myc tag, tandem mCherry-GFP tag were used to express various fusion proteins. For tandem affinity purification (TAP), entry plasmids were subsequently recombined into a lentiviral gateway-compatible destination vector for the expression of SFB-tagged fusion proteins. PCR-based mutagenesis was used to generate the indicated site mutations. The pEntry-FYCO1 construct was kindly provided by Dr. Terje Johansen (University of Tromsø, Norway).

The MAP4K2 pLKO.1 shRNAs were purchased from Sigma-Aldrich. The sequence information of MAP4K2 shRNAs used for MAP4K2 knockdown studies is as follows:

MAP4K2 shRNA-1#: CAGTTTCACCAGGTGAAATTT (#TRCN0000195052);

MAP4K2 shRNA-2#: CGCCTGCTTCTCCAAGGTCTT (#TRCN0000199054);

Control shRNA: CCTAAGGTTAAGTCGCCCTCG (Addgene plasmid # 136035).

Lentiviral supernatants were generated by transient transfection of HEK293T cells with the helper plasmids pSPAX2 and pMD2G (kindly provided by Dr. Zhou Songyang, Baylor College of Medicine) and harvested 48 hours later. Supernatants were passed through a 0.45-μm filter and used to infect cells with the addition of 8 μg/mL hexadimethrine bromide (Polybrene) (Sigma-Aldrich). Plasmid transfection was performed using a polyethyleneimine (PEI) reagent.

Tandem Affinity Purification Coupled with Mass Spectrometry (TAP-MS) Analysis—The TAP-MS analysis was performed as described previously[18,69]. Briefly, HEK293T cells stably expressing SFB-tagged MAP4K2 and the indicated ATG8-family proteins were generated by culturing in medium containing 2 μg/mL puromycin and validated by immunostaining and Western blotting. The HEK293T stable cells were lysed in NETN buffer containing protease and phosphatase inhibitors at 4 °C for 20 minutes. The

crude lysates were centrifuged at 13,000 rpm for 15 minutes at 4 °C. The supernatants were incubated with streptavidin-conjugated beads (GE Healthcare) at 4 °C for 4~6 hours. The beads were then washed 3 times with NETN buffer, and the bound proteins were eluted with NETN buffer containing 2 mg/mL biotin (Sigma-Aldrich) at 4 °C overnight. The elutes were incubated with S protein beads (Novagen) at 4 °C for 4 hours. The beads were washed three times with NETN buffer and subjected to sodium dodecyl sulfate polyacrylamide gel electrophoresis (SDS-PAGE). Each sample was run into the separation gel for a short distance, so that the whole bands could be excised as one sample.

The excised gel sample was cut into approximately 1-mm^3 pieces. The gel pieces were then subjected to in-gel trypsin digestion[70] and dried. Samples were reconstituted in 5 μL of high-performance liquid chromatography (HPLC) solvent A (2.5% acetonitrile, 0.1% formic acid). A nanoscale reverse-phase HPLC capillary column was created by packing 5-μm C18 spherical silica beads into a fused silica capillary (100 μm inner diameter × ~20 cm length) with a flame-drawn tip. After the column was equilibrated, each sample was loaded onto the column via a Famos autosampler (LC Packings). A gradient was formed, and peptides were eluted with increasing concentrations of solvent B (97.5% acetonitrile, 0.1% formic acid). As the peptides eluted, they were subjected to electrospray ionization and then entered into an LTQ Orbitrap Elite mass spectrometer (Thermo Fisher Scientific). The peptides were detected, isolated, and fragmented to produce a tandem mass spectrum of specific fragment ions for each peptide. Peptide sequences (and hence protein identity) were determined by matching protein databases with the fragmentation pattern acquired by the software program SEQUEST (ver. 28) (Thermo Fisher Scientific). Enzyme specificity was set to partially tryptic with 2 missed cleavages. Modifications included carboxyamidomethyl (cysteines, fixed) and oxidation (methionine, variable). Mass tolerance was set to 5 ppm for precursor ions and 0.5 Da for fragment ions. The database searched was UniProt. Spectral matches were filtered to contain a false discovery rate of less than 1% at the peptide level using the target-decoy method[71], a simple and powerful way to deliver false positive estimations applied to MS/MS workflow. The protein inference was considered followed the general rules[72] with manual annotation based on experience applied when necessary. Briefly, computational tools, protein sequence databases, identification of mature forms of proteins, quantitative proteomics, integration of proteomic and transcriptional data, integration of multiple shotgun proteomic datasets and gene-centered data interpretation were considered for protein inference. This same principle was used for isoforms when they were present in the database. The longest isoform was reported as the match.

Immunofluorescent Staining—Immunofluorescent staining was performed as described previously[73]. Briefly, cells cultured on coverslips were fixed with 4% paraformaldehyde for 10 minutes at room temperature and then extracted with 0.5% Triton X-100 solution for 5 minutes. After blocking with Tris-buffered saline with Tween 20 containing 1% bovine serum albumin, the cells were incubated with the indicated primary antibodies for 1 hour at room temperature. After that, the cells were washed and incubated with fluorescein isothiocyanate-, rhodamine- or Cy5-conjugated secondary antibodies for 1 hour. Cells were counterstained with 100 ng/mL 4′,6-diamidino-2-phenylindole (Dapi) for 2 minutes to

visualize nuclear DNA. The cover slips were mounted onto glass slides with an anti-fade solution and visualized under a Nikon Ti2-E inverted microscope.

Gene Inactivation by the CRISPR/Cas9 System—To generate knockout cells, five distinct single-guide RNAs (sgRNA) were designed by CHOPCHOP website (https://chopchop.rc.fas.harvard.edu), cloned into lentiGuide-Puro vector (Addgene plasmid # 52963), and transfected into HEK293A cells with lentiCas9-Blast construct (Addgene plasmid # 52962). The next day, cells were transiently selected with puromycin (2 μg/ml) for two days and sub-cloned to form single colonies. Knockout cell clones were screened by Western blot to verify the loss of target protein expression. The MST/MAP4K-8KO HEK293A cells were kindly provided by Dr. Kun-Liang Guan (University of California, San Diego). The STRN4 KO HEK293A cells were generated as described previously[11]. The sequence information for sgRNAs used for MAP4K2 knockout cell generation is as follows:

MAP4K2_sgRNA1: TGTAGGCCACCACATTGGGG;

MAP4K2_sgRNA2: ATGTGTCGCTGCAGGACCCG;

MAP4K2_sgRNA3: GCGACGTCTACAAGGTGCGA;

MAP4K2_sgRNA4: GTAGACGTCGCCATAGGTCC;

MAP4K2_sgRNA5: TCTACAAGGTGCGACGGGAC.

Transmission Electron Microscopy (TEM) Analysis—Cells were primarily fixed with paraformaldehyde/glutaraldehyde and followed by OsO4. After washing, cells were dehydrated, washed three times with 100% ethanol, and incubated with propylene:resin solution (50:50, v/v) overnight at room temperature. Cells were further incubated with the propylene:resin solution (50:50, v/v) for another two hours to evaporate propylene oxide. After that, cells were incubated with 100% resin at 60 °C for two days. The cell sections (120 nm) were processed using a ultramicrotome (EM UC7, Leica Microsystems GmbH, Vienna) and sequentially stained with uranyl acetate and lead citrate before imaging under a transmission electron microscope (JEM-2100F, JEOL USA). The images were captured using a CCD digital camera (OneView, Gatan Inc, USA). To produce the picture of whole cell morphology, multiple images were first acquired as a stack of frames by *SerialEM* and then stitched into a montage using *IMOD* software package (IMOD, University of Colorado, USA).

Oil Red O Staining—Fresh liver samples were collected in OCT compound, rapidly frozen in a dry ice-ethanol bath, and processed as frozen sections by UCI Experimental Tissue Resource (ETR) facility. The frozen sections were air-dried for 60 min at room temperature and fixed in ice cold 10% formalin for 10 min. The tissue slides were then washed with 60% isopropanol, stained with oil red O solution for 15 min, counterstained with hematoxylin, and washed with distilled water.

***In Vitro* Kinase Assay—**SFB-MAP4K2 or its mutant (i.e., K45R, S170A and ΔLIR) was expressed in HEK293T cells and purified using S protein beads. The isolated kinase was

washed three times in washing buffer (40mM HEPES and 250 mM NaCl) and once in kinase buffer (30 mM HEPES, 50 mM potassium acetate and 5 mM MgCl2), and subjected to the kinase assay in the presence of cold ATP (500 μM). Bacterially purified GST-tagged ATG8-family proteins and their indicated mutants or MBP-LATS1-C3 were used as substrates. The reaction mixture was incubated at 30 °C for 30 min, terminated with SDS loading buffer, and subjected to SDS-PAGE. The MAP4K2-induced LC3A phosphorylation was examined using anti-phospho-LC3A (S87) antibody. Phosphorylation of LATS1-hydrophobic motif (HM) was determined by anti-phospho-LATS1 (T1079) antibody. To make phos-tag gel, 60 μL 5 mM phos-tag acrylamide (AAL-107, FUJIFILM Wako Chemicals) prepared in 3% (v/v) methanol and 120 μL 10 mM MnCl2 solution were added into 12 mL regular 7.5% acrylamide resolving gel solution. Protein samples were loaded into regular stacking gel and phos-tag-containing resolving gel for SDS-PAGE analysis.

Phosphorylation Site Analysis by Liquid Chromatography Tandem Mass Spectrometry (LC MS/MS)—To identify the MAP4K2 phosphorylation site on LC3A, bacterially expressed and purified GST-LC3A protein was subjected to MAP4K2 *in vitro* kinase assay as substrate and analyzed by mass spectrometry. Chymotrypsin (V106A) was purchased from Promega and used for protein digestion. Peptide digests were analyzed by LC MS/MS utilizing an UltiMate 3000 UHPLC (Thermo Fisher Scientific) coupled on-line to an Orbitrap Fusion Lumos mass spectrometer (Thermo Fisher Scientific) as previously described[74]. Protein identification and phosphorylation characterization were done with database searching using Protein Prospector. All MS/MS spectra for phosphorylated peptides were further inspected manually.

Immunohistochemical Analysis—The head and neck cancer tissue arrays (HN802c and HN242b) were purchased from US Biomax, Inc. According to the Declaration of Specimen Collection provided by US Biomax, each specimen collected from any clinic was consented by both hospital and individual.

The head and neck cancer tissue arrays were deparaffinized and rehydrated. The antigens were retrieved by applying Unmask Solution (Vector Laboratories) in a steamer for 40 min. To block endogenous peroxidase activity, the sections were treated with 3% hydrogen peroxide for 30 min. After one hour of pre-incubation in 10% goat serum to prevent non-specific staining, the samples were incubated with an antibody at 4 °C overnight. The sections were incubated with SignalStain Boost detection reagent at room temperature for 30 min. Color was developed with SignalStain 3,3’-diaminobenzidine chromogen-diluted solution (all reagents were obtained from Cell Signaling Technology). Sections were counterstained with Mayer hematoxylin. To quantify the results, a total score of protein expression was calculated from both the percentage of immunopositive cells and immunostaining intensity. High and low protein expressions were defined using the mean score of all samples as a cutoff point. Pearson chi-square analysis test was used for statistical analysis with tissue type (normal versus tumor).

Animal Studies—The lipid droplet study was followed institutional guidelines, approved by the Institutional Animal Care and Use Committee (IACUC; protocol number AUP-19-112) of the University of California, Irvine, and performed under veterinary

supervision. Specifically, four-week-old female C57BL/6 mice were intraperitoneally injected with vehicle control or TL4-12 (15 mg/kg) once a day for a week and then fasted for 16 hours. Mouse liver tissues were collected and fixed in formalin and OCT compound for histological study and oil red O staining, respectively.

The orthotopic xenograft tumor experiments were followed institutional guidelines, approved by the Institutional Animal Care and Use Committee (IACUC; protocol number AUP-19-112) of the University of California, Irvine, and performed under veterinary supervision. The indicated CAL-27 cells (0.5×10^6) were injected into the tongue tissues of eight-week-old female nude mice. Mice were euthanized for tumor collection and analysis around 15~17 days post injection. As for the TL4-12 treatment experiments, eight-week-old female nude mice were randomly assigned to groups for the indicated cell injections and treatments. As for the treatment, vehicle control or TL4–12 (15 mg/kg) were intraperitoneally injected once a day for a week and then every other day for another week. The tumor volume was calculated using the standard formula V=length × width^2/2.

The patient-derived xenograft (PDX) tumor experiments were followed institutional guidelines, approved by the Institutional Animal Care and Use Committee (IACUC; protocol number L025501202212006) of Sun Yat-sen University Cancer Center, and performed under veterinary supervision. Tumor tissues obtained from two cancer patients with tongue squamous carcinoma were developed into the two patient-derived xenografts (PDX) lines (Sun Yat-sen University Cancer Center). The PDX lines were implanted into the flank of six-week-old female NOD-SCID-IL2rg (NSG) mice for the PDX tumor study as previously described[75]. When tumors became palpable, the tumor-bearing mice were randomly assigned to two groups (5 mice per group). As for the treatment, vehicle control or TL4-12 (15 mg/kg) were intraperitoneally injected once a day for a week and then every other day for another two weeks. Tumor size was measured every 3 days using a caliper, and tumor volume was calculated using the standard formula V=length × width^2/2.

Quantification and Statistical Analysis—Each experiment was repeated twice or more, unless otherwise noted. There were no samples excluded for the analyses in this study. The Student's *t*-test was used to analyze the differences between groups. Data were analyzed by Student's *t*-test, Pearson chi-square analysis, or log-rank (Mantel-Cox) test. SD was used for error estimation. p value < 0.05 was considered statistically significant.

Supplementary Material

Refer to Web version on PubMed Central for supplementary material.

Acknowledgments

We thank Dr. Ross Tomaino (Taplin Mass Spectrometry Facility, Harvard Medical School) for the mass spectrometry analysis, Drs. Xuejun Jiang (Memorial Sloan Kettering Cancer Center) and Grant MacGregor (University of California, Irvine) for insightful comments on this study, and Dr. Justin WC Leung (The University of Texas at San Antonio) for technical help. The authors acknowledge the use of service and instrumentation at the UCI Materials Research Institute (IMRI) supported in part by the National Science Foundation through the UCI Materials Research Science and Engineering Center (DMR-2011967) and the UCI Experimental Tissue Resource (ETR) facility. This work was supported by NIH grants (R01GM126048, R01GM143233) and American Cancer Society Research Scholar Award (RSG-18-009-01-CCG) to W.W. and NIH grant (R35GM145249) to L.H..

Research reported in this publication was also supported in part by NIH grant (P30CA062203) and the UCI Chao Family Comprehensive Cancer Center using Anti-Cancer Challenge funds.

References

1. Yu FX, Zhao B, and Guan KL (2015). Hippo Pathway in Organ Size Control, Tissue Homeostasis, and Cancer. Cell 163, 811–828. 10.1016/j.cell.2015.10.044.
2. Ma S, Meng Z, Chen R, and Guan KL (2019). The Hippo Pathway: Biology and Pathophysiology. Annu Rev Biochem 88, 577–604. 10.1146/annurev-biochem-013118-111829. [PubMed: 30566373]
3. Zheng Y, and Pan D. (2019). The Hippo Signaling Pathway in Development and Disease. Dev Cell 50, 264–282. 10.1016/j.devcel.2019.06.003. [PubMed: 31386861]
4. Halder G, and Johnson RL (2011). Hippo signaling: growth control and beyond. Development 138, 9–22. 10.1242/dev.045500. [PubMed: 21138973]
5. Zheng Y, Wang W, Liu B, Deng H, Uster E, and Pan D. (2015). Identification of Happyhour/MAP4K as Alternative Hpo/Mst-like Kinases in the Hippo Kinase Cascade. Dev Cell 34, 642–655. 10.1016/j.devcel.2015.08.014. [PubMed: 26364751]
6. Li S, Cho YS, Yue T, Ip YT, and Jiang J. (2015). Overlapping functions of the MAP4K family kinases Hppy and Msn in Hippo signaling. Cell Discov 1, 15038. 10.1038/celldisc.2015.38. [PubMed: 27462435]
7. Meng Z, Moroishi T, Mottier-Pavie V, Plouffe SW, Hansen CG, Hong AW, Park HW, Mo JS, Lu W, Lu S, et al. (2015). MAP4K family kinases act in parallel to MST1/2 to activate LATS1/2 in the Hippo pathway. Nat Commun 6, 8357. 10.1038/ncomms9357. [PubMed: 26437443]
8. Li Q, Li S, Mana-Capelli S, Roth Flach RJ, Danai LV, Amcheslavsky A, Nie Y, Kaneko S, Yao X, Chen X, et al. (2014). The conserved misshapen-warts-Yorkie pathway acts in enteroblasts to regulate intestinal stem cells in Drosophila. Dev Cell 31, 291–304. 10.1016/j.devcel.2014.09.012. [PubMed: 25453828]
9. Li Q, Nirala NK, Nie Y, Chen HJ, Ostroff G, Mao J, Wang Q, Xu L, and Ip YT (2018). Ingestion of Food Particles Regulates the Mechanosensing Misshapen-Yorkie Pathway in Drosophila Intestinal Growth. Dev Cell 45, 433–449 e436. 10.1016/j.devcel.2018.04.014. [PubMed: 29754801]
10. Zheng Y, Liu B, Wang L, Lei H, Pulgar Prieto KD, and Pan D. (2017). Homeostatic Control of Hpo/MST Kinase Activity through Autophosphorylation-Dependent Recruitment of the STRIPAK PP2A Phosphatase Complex. Cell Rep 21, 3612–3623. 10.1016/j.celrep.2017.11.076. [PubMed: 29262338]
11. Seo G, Han H, Vargas RE, Yang B, Li X, and Wang W. (2020). MAP4K Interactome Reveals STRN4 as a Key STRIPAK Complex Component in Hippo Pathway Regulation. Cell Rep 32, 107860. 10.1016/j.celrep.2020.107860.
12. DeRan M, Yang J, Shen CH, Peters EC, Fitamant J, Chan P, Hsieh M, Zhu S, Asara JM, Zheng B, et al. (2014). Energy stress regulates hippo-YAP signaling involving AMPK-mediated regulation of angiomotin-like 1 protein. Cell Rep 9, 495–503. 10.1016/j.celrep.2014.09.036. [PubMed: 25373897]
13. Wang W, Xiao ZD, Li X, Aziz KE, Gan B, Johnson RL, and Chen J. (2015). AMPK modulates Hippo pathway activity to regulate energy homeostasis. Nat Cell Biol 17, 490–499. 10.1038/ncb3113. [PubMed: 25751139]
14. Mo JS, Meng Z, Kim YC, Park HW, Hansen CG, Kim S, Lim DS, and Guan KL (2015). Cellular energy stress induces AMPK-mediated regulation of YAP and the Hippo pathway. Nat Cell Biol 17, 500–510. 10.1038/ncb3111. [PubMed: 25751140]
15. Gailite I, Aerne BL, and Tapon N. (2015). Differential control of Yorkie activity by LKB1/AMPK and the Hippo/Warts cascade in the central nervous system. Proc Natl Acad Sci U S A 112, E5169–5178. 10.1073/pnas.1505512112. [PubMed: 26324895]
16. Zheng X, Han H, Liu GP, Ma YX, Pan RL, Sang LJ, Li RH, Yang LJ, Marks JR, Wang W, and Lin A. (2017). LncRNA wires up Hippo and Hedgehog signaling to reprogramme glucose metabolism. EMBO J 36, 3325–3335. 10.15252/embj.201797609. [PubMed: 28963395]
17. Garcia D, and Shaw RJ (2017). AMPK: Mechanisms of Cellular Energy Sensing and Restoration of Metabolic Balance. Mol Cell 66, 789–800. 10.1016/j.molcel.2017.05.032. [PubMed: 28622524]

18. Wang W, Li X, Huang J, Feng L, Dolinta KG, and Chen J. (2014). Defining the protein-protein interaction network of the human hippo pathway. Mol Cell Proteomics 13, 119–131. 10.1074/mcp.M113.030049. [PubMed: 24126142]
19. Couzens AL, Knight JD, Kean MJ, Teo G, Weiss A, Dunham WH, Lin ZY, Bagshaw RD, Sicheri F, Pawson T, et al. (2013). Protein interaction network of the mammalian Hippo pathway reveals mechanisms of kinase-phosphatase interactions. Sci Signal 6, rs15. 10.1126/scisignal.2004712.
20. Hauri S, Wepf A, van Drogen A, Varjosalo M, Tapon N, Aebersold R, and Gstaiger M. (2013). Interaction proteome of human Hippo signaling: modular control of the co-activator YAP1. Mol Syst Biol 9, 713. 10.1002/msb.201304750. [PubMed: 24366813]
21. Parzych KR, and Klionsky DJ (2014). An overview of autophagy: morphology, mechanism, and regulation. Antioxid Redox Signal 20, 460–473. 10.1089/ars.2013.5371. [PubMed: 23725295]
22. Zhao YG, Codogno P, and Zhang H. (2021). Machinery, regulation and pathophysiological implications of autophagosome maturation. Nat Rev Mol Cell Biol 22, 733–750. 10.1038/s41580-021-00392-4. [PubMed: 34302147]
23. Russell RC, and Guan KL (2022). The multifaceted role of autophagy in cancer. EMBO J 41, e110031. 10.15252/embj.2021110031.
24. Han H, Qi R, Zhou JJ, Ta AP, Yang B, Nakaoka HJ, Seo G, Guan KL, Luo R, and Wang W. (2018). Regulation of the Hippo Pathway by Phosphatidic Acid-Mediated Lipid-Protein Interaction. Mol Cell 72, 328–340 e328. 10.1016/j.molcel.2018.08.038. [PubMed: 30293781]
25. Fujita N, Itoh T, Omori H, Fukuda M, Noda T, and Yoshimori T. (2008). The Atg16L complex specifies the site of LC3 lipidation for membrane biogenesis in autophagy. Mol Biol Cell 19, 2092–2100. 10.1091/mbc.E07-12-1257. [PubMed: 18321988]
26. Xiong Q, Li W, Li P, Yang M, Wu C, and Eichinger L. (2018). The Role of ATG16 in Autophagy and The Ubiquitin Proteasome System. Cells 8. 10.3390/cells8010002.
27. Itakura E, Kishi-Itakura C, and Mizushima N. (2012). The hairpin-type tail-anchored SNARE syntaxin 17 targets to autophagosomes for fusion with endosomes/lysosomes. Cell 151, 1256–1269. 10.1016/j.cell.2012.11.001. [PubMed: 23217709]
28. Kimura S, Noda T, and Yoshimori T. (2007). Dissection of the autophagosome maturation process by a novel reporter protein, tandem fluorescent-tagged LC3. Autophagy 3, 452–460. 10.4161/auto.4451. [PubMed: 17534139]
29. Mizushima N, Yoshimori T, and Levine B. (2010). Methods in mammalian autophagy research. Cell 140, 313–326. 10.1016/j.cell.2010.01.028. [PubMed: 20144757]
30. McEwan DG, Popovic D, Gubas A, Terawaki S, Suzuki H, Stadel D, Coxon FP, Miranda de Stegmann D, Bhogaraju S, Maddi K, et al. (2015). PLEKHM1 regulates autophagosome-lysosome fusion through HOPS complex and LC3/GABARAP proteins. Mol Cell 57, 39–54. 10.1016/j.molcel.2014.11.006. [PubMed: 25498145]
31. Nakamura S, and Yoshimori T. (2017). New insights into autophagosome-lysosome fusion. J Cell Sci 130, 1209–1216. 10.1242/jcs.196352. [PubMed: 28302910]
32. Pankiv S, Alemu EA, Brech A, Bruun JA, Lamark T, Overvatn A, Bjorkoy G, and Johansen T. (2010). FYCO1 is a Rab7 effector that binds to LC3 and PI3P to mediate microtubule plus end-directed vesicle transport. J Cell Biol 188, 253–269. 10.1083/jcb.200907015. [PubMed: 20100911]
33. Pankiv S, and Johansen T. (2010). FYCO1: linking autophagosomes to microtubule plus end-directing molecular motors. Autophagy 6, 550–552. 10.4161/auto.6.4.11670. [PubMed: 20364109]
34. Aligianis IA, Johnson CA, Gissen P, Chen D, Hampshire D, Hoffmann K, Maina EN, Morgan NV, Tee L, Morton J, et al. (2005). Mutations of the catalytic subunit of RAB3GAP cause Warburg Micro syndrome. Nat Genet 37, 221–223. 10.1038/ng1517. [PubMed: 15696165]
35. Morris-Rosendahl DJ, Segel R, Born AP, Conrad C, Loeys B, Brooks SS, Muller L, Zeschnigk C, Botti C, Rabinowitz R, et al. (2010). New RAB3GAP1 mutations in patients with Warburg Micro Syndrome from different ethnic backgrounds and a possible founder effect in the Danish. Eur J Hum Genet 18, 1100–1106. 10.1038/ejhg.2010.79. [PubMed: 20512159]
36. Borck G, Wunram H, Steiert A, Volk AE, Korber F, Roters S, Herkenrath P, Wollnik B, Morris-Rosendahl DJ, and Kubisch C. (2011). A homozygous RAB3GAP2 mutation causes Warburg Micro syndrome. Hum Genet 129, 45–50. 10.1007/s00439-010-0896-2. [PubMed: 20967465]

37. Spang N, Feldmann A, Huesmann H, Bekbulat F, Schmitt V, Hiebel C, Koziollek-Drechsler I, Clement AM, Moosmann B, Jung J, et al. (2014). RAB3GAP1 and RAB3GAP2 modulate basal and rapamycin-induced autophagy. Autophagy 10, 2297–2309. 10.4161/15548627.2014.994359. [PubMed: 25495476]
38. Feldmann A, Bekbulat F, Huesmann H, Ulbrich S, Tatzelt J, Behl C, and Kern A. (2017). The RAB GTPase RAB18 modulates macroautophagy and proteostasis. Biochem Biophys Res Commun 486, 738–743. 10.1016/j.bbrc.2017.03.112. [PubMed: 28342870]
39. Takats S, Levay L, Boda A, Toth S, Simon-Vecsei Z, Rubics A, Varga A, Lippai M, Lorincz P, Glatz G, and Juhasz G. (2021). The Warburg Micro Syndrome-associated Rab3GAP-Rab18 module promotes autolysosome maturation through the Vps34 Complex I. FEBS J 288, 190–211. 10.1111/febs.15313. [PubMed: 32248620]
40. Gerondopoulos A, Bastos RN, Yoshimura S, Anderson R, Carpanini S, Aligianis I, Handley MT, and Barr FA (2014). Rab18 and a Rab18 GEF complex are required for normal ER structure. J Cell Biol 205, 707–720. 10.1083/jcb.201403026. [PubMed: 24891604]
41. Gatti A, Huang Z, Tuazon PT, and Traugh JA (1999). Multisite autophosphorylation of p21-activated protein kinase gamma-PAK as a function of activation. J Biol Chem 274, 8022–8028. 10.1074/jbc.274.12.8022. [PubMed: 10075701]
42. Glantschnig H, Rodan GA, and Reszka AA (2002). Mapping of MST1 kinase sites of phosphorylation. Activation and autophosphorylation. J Biol Chem 277, 42987–42996. 10.1074/jbc.M208538200. [PubMed: 12223493]
43. Quintero OA, Unrath WC, Stevens SM Jr., Manor U, Kachar B, and Yengo CM (2013). Myosin 3A kinase activity is regulated by phosphorylation of the kinase domain activation loop. J Biol Chem 288, 37126–37137. 10.1074/jbc.M113.511014. [PubMed: 24214986]
44. Cybulsky AV, Guillemette J, Papillon J, and Abouelazm NT (2017). Regulation of Ste20-like kinase, SLK, activity: Dimerization and activation segment phosphorylation. PLoS One 12, e0177226. 10.1371/journal.pone.0177226. [PubMed: 28475647]
45. Praskova M, Khoklatchev A, Ortiz-Vega S, and Avruch J. (2004). Regulation of the MST1 kinase by autophosphorylation, by the growth inhibitory proteins, RASSF1 and NORE1, and by Ras. Biochem J 381, 453–462. 10.1042/BJ20040025. [PubMed: 15109305]
46. White E. (2015). The role for autophagy in cancer. J Clin Invest 125, 42–46. 10.1172/JCI73941. [PubMed: 25654549]
47. Levy JMM, Towers CG, and Thorburn A. (2017). Targeting autophagy in cancer. Nat Rev Cancer 17, 528–542. 10.1038/nrc.2017.53. [PubMed: 28751651]
48. Amaravadi RK, Kimmelman AC, and Debnath J. (2019). Targeting Autophagy in Cancer: Recent Advances and Future Directions. Cancer Discov 9, 1167–1181. 10.1158/2159-8290.CD-19-0292. [PubMed: 31434711]
49. Mulcahy Levy JM, and Thorburn A. (2020). Autophagy in cancer: moving from understanding mechanism to improving therapy responses in patients. Cell Death Differ 27, 843–857. 10.1038/s41418-019-0474-7. [PubMed: 31836831]
50. Chen R, Xie R, Meng Z, Ma S, and Guan KL (2019). STRIPAK integrates upstream signals to initiate the Hippo kinase cascade. Nat Cell Biol 21, 1565–1577. 10.1038/s41556-019-0426-y. [PubMed: 31792377]
51. Nian FS, Li LL, Cheng CY, Wu PC, Lin YT, Tang CY, Ren BS, Tai CY, Fann MJ, Kao LS, et al. (2019). Rab18 Collaborates with Rab7 to Modulate Lysosomal and Autophagy Activities in the Nervous System: an Overlapping Mechanism for Warburg Micro Syndrome and Charcot-Marie-Tooth Neuropathy Type 2B. Mol Neurobiol 56, 6095–6105. 10.1007/s12035-019-1471-z. [PubMed: 30721447]
52. Hubert V, Peschel A, Langer B, Groger M, Rees A, and Kain R. (2016). LAMP-2 is required for incorporating syntaxin-17 into autophagosomes and for their fusion with lysosomes. Biol Open 5, 1516–1529. 10.1242/bio.018648. [PubMed: 27628032]
53. Hyttinen JM, Niittykoski M, Salminen A, and Kaarniranta K. (2013). Maturation of autophagosomes and endosomes: a key role for Rab7. Biochim Biophys Acta 1833, 503–510. 10.1016/j.bbamcr.2012.11.018. [PubMed: 23220125]

54. Ishihara N, Hamasaki M, Yokota S, Suzuki K, Kamada Y, Kihara A, Yoshimori T, Noda T, and Ohsumi Y. (2001). Autophagosome requires specific early Sec proteins for its formation and NSF/SNARE for vacuolar fusion. Mol Biol Cell 12, 3690–3702. 10.1091/mbc.12.11.3690. [PubMed: 11694599]
55. Ghislat G, and Knecht E. (2013). Ca(2)(+)-sensor proteins in the autophagic and endocytic traffic. Curr Protein Pept Sci 14, 97–110. 10.2174/13892037112139990033. [PubMed: 23305313]
56. Wilkinson DS, Jariwala JS, Anderson E, Mitra K, Meisenhelder J, Chang JT, Ideker T, Hunter T, Nizet V, Dillin A, and Hansen M. (2015). Phosphorylation of LC3 by the Hippo kinases STK3/STK4 is essential for autophagy. Mol Cell 57, 55–68. 10.1016/j.molcel.2014.11.019. [PubMed: 25544559]
57. Nieto-Torres JL, Shanahan SL, Chassefeyre R, Chaiamarit T, Zaretski S, Landeras-Bueno S, Verhelle A, Encalada SE, and Hansen M. (2021). LC3B phosphorylation regulates FYCO1 binding and directional transport of autophagosomes. Curr Biol 31, 3440–3449 e3447. 10.1016/j.cub.2021.05.052. [PubMed: 34146484]
58. Maejima Y, Kyoi S, Zhai P, Liu T, Li H, Ivessa A, Sciarretta S, Del Re DP, Zablocki DK, Hsu CP, et al. (2013). Mst1 inhibits autophagy by promoting the interaction between Beclin1 and Bcl-2. Nat Med 19, 1478–1488. 10.1038/nm.3322. [PubMed: 24141421]
59. Li W, Yue F, Dai Y, Shi B, Xu G, Jiang X, Zhou X, Pfeifer GP, and Liu L. (2019). Suppressor of hepatocellular carcinoma RASSF1A activates autophagy initiation and maturation. Cell Death Differ 26, 1379–1395. 10.1038/s41418-018-0211-7. [PubMed: 30315205]
60. Pavel M, Renna M, Park SJ, Menzies FM, Ricketts T, Fullgrabe J, Ashkenazi A, Frake RA, Lombarte AC, Bento CF, et al. (2018). Contact inhibition controls cell survival and proliferation via YAP/TAZ-autophagy axis. Nat Commun 9, 2961. 10.1038/s41467-018-05388-x. [PubMed: 30054475]
61. Totaro A, Zhuang Q, Panciera T, Battilana G, Azzolin L, Brumana G, Gandin A, Brusatin G, Cordenonsi M, and Piccolo S. (2019). Cell phenotypic plasticity requires autophagic flux driven by YAP/TAZ mechanotransduction. Proc Natl Acad Sci U S A 116, 17848–17857. 10.1073/pnas.1908228116. [PubMed: 31416916]
62. Cherra SJ 3rd, Kulich SM, Uechi G, Balasubramani M, Mountzouris J, Day BW, and Chu CT (2010). Regulation of the autophagy protein LC3 by phosphorylation. J Cell Biol 190, 533–539. 10.1083/jcb.201002108. [PubMed: 20713600]
63. Kudo Y, Sugimoto M, Arias E, Kasashima H, Cordes T, Linares JF, Duran A, Nakanishi Y, Nakanishi N, L'Hermitte A, et al. (2020). PKClambda/iota Loss Induces Autophagy, Oxidative Phosphorylation, and NRF2 to Promote Liver Cancer Progression. Cancer Cell 38, 247–262 e211. 10.1016/j.ccell.2020.05.018. [PubMed: 32589943]
64. Schaaf MB, Keulers TG, Vooijs MA, and Rouschop KM (2016). LC3/GABARAP family proteins: autophagy-(un)related functions. FASEB J 30, 3961–3978. 10.1096/fj.201600698R. [PubMed: 27601442]
65. Rikiishi H. (2012). Autophagic action of new targeting agents in head and neck oncology. Cancer Biol Ther 13, 978–991. 10.4161/cbt.21079. [PubMed: 22825332]
66. Sannigrahi MK, Singh V, Sharma R, Panda NK, and Khullar M. (2015). Role of autophagy in head and neck cancer and therapeutic resistance. Oral Dis 21, 283–291. 10.1111/odi.12254. [PubMed: 24797102]
67. Li C, Wu ZH, and Yuan K. (2020). Autophagy-Related Signature for Head and Neck Squamous Cell Carcinoma. Dis Markers 2020, 8899337. 10.1155/2020/8899337.
68. Wang W, Huang J, and Chen J. (2011). Angiomotin-like proteins associate with and negatively regulate YAP1. J Biol Chem 286, 4364–4370. 10.1074/jbc.C110.205401. [PubMed: 21187284]
69. Li X, Tran KM, Aziz KE, Sorokin AV, Chen J, and Wang W. (2016). Defining the Protein-Protein Interaction Network of the Human Protein Tyrosine Phosphatase Family. Mol Cell Proteomics 15, 3030–3044. 10.1074/mcp.M116.060277. [PubMed: 27432908]
70. Shevchenko A, Wilm M, Vorm O, and Mann M. (1996). Mass spectrometric sequencing of proteins silver-stained polyacrylamide gels. Anal Chem 68, 850–858. [PubMed: 8779443]

71. Elias JE, and Gygi SP (2007). Target-decoy search strategy for increased confidence in large-scale protein identifications by mass spectrometry. Nat Methods 4, 207–214. nmeth1019 [pii] 10.1038/nmeth1019. [PubMed: 17327847]

72. Nesvizhskii AI, and Aebersold R. (2005). Interpretation of shotgun proteomic data: the protein inference problem. Mol Cell Proteomics 4, 1419–1440. R500012-MCP200 [pii] 10.1074/mcp.R500012-MCP200. [PubMed: 16009968]

73. Wang W, Chen L, Ding Y, Jin J, and Liao K. (2008). Centrosome separation driven by actin-microfilaments during mitosis is mediated by centrosome-associated tyrosine-phosphorylated cortactin. J Cell Sci 121, 1334–1343. 10.1242/jcs.018176 121/8/1334 [pii]. [PubMed: 18388321]

74. Wang X, Chemmama IE, Yu C, Huszagh A, Xu Y, Viner R, Block SA, Cimermancic P, Rychnovsky SD, Ye Y, et al. (2017). The proteasome-interacting Ecm29 protein disassembles the 26S proteasome in response to oxidative stress. J Biol Chem 292, 16310–16320. 10.1074/jbc.M117.803619. [PubMed: 28821611]

75. Wang Y, Lu JH, Wang F, Wang YN, He MM, Wu QN, Lu YX, Yu HE, Chen ZH, Zhao Q, et al. (2020). Inhibition of fatty acid catabolism augments the efficacy of oxaliplatin-based chemotherapy in gastrointestinal cancers. Cancer Lett 473, 74–89. 10.1016/j.canlet.2019.12.036. [PubMed: 31904482]

Highlights

- Hippo kinase MAP4K2 drives autophagy and cell survival upon energy stress
- MAP4K2 phosphorylates LC3A at S87 to drive autophagic flux
- Energy stress targets the MAP4K2-STRIPAK^{STRN4} complex formation to activate MAP4K2
- MAP4K2-mediated autophagy is required for head and neck cancer development

A

Bait: MAP4K2	
70/803	MAP4K2
50/67	DHX9
25/25	AP3B1
22/24	PLEKHA5
18/18	ASCC3
17/21	G3BP1
17/17	YTHDC2
13/13	AP3D1
9/10	G3BP2
8/8	PIP5K1A
7/8	GABARAPL2
6/8	YTHDF2
6/6	YTHDF1
4/6	GABARAP
4/5	GSK3B
2/3	GABARAPL1
1/1	STAU1
Unique/Total	Prey

Bait: MAP1LC3A	
73/91	FYCO1
36/38	USP28
35/37	RAB3GAP1
34/35	AKAP11
30/46	ATG7
30/34	RAP3GAP2
23/44	ATG4B
21/37	SQSTM1
20/21	MAP1B
12/14	KEAP1
9/9	TBC1D15
8/8	MAP4K2
7/7	ATG16L1
6/10	ATG3
6/6	ATG4A
5/10	MAP1LC3A
2/2	ATG5
Unique/Total	Prey

Bait: MAP1LC3B	
116/150	FYCO1
56/173	ATG7
55/107	ATG16L1
51/51	MAP1B
30/46	ATG7
29/69	ATG3
25/57	SQSTM1
24/68	ATG4B
23/23	AKAP11
22/23	USP28
21/26	ATG5
15/17	KEAP1
11/131	MAP1LC3B
6/11	ATG12
4/4	ATG4A
2/2	MAP4K2
2/2	RAB3GAP1
Unique/Total	Prey

Bait: GABARAPL1	
39/44	TBC1D2B
34/80	ATG7
33/143	RABGAP1
26/27	AKAP11
16/22	SQSTM1
15/15	RAB3GAP2
13/13	MAP4K2
13/13	RABGAP1L
11/11	ATG16L1
11/11	USP28
11/11	RAB3GAP1
8/8	TBC1D15
4/5	ATG4C
4/5	GABARAPL1
4/4	ATG5
2/2	SKP1
1/1	ATG12
Unique/Total	Prey

Bait: GABARAPL2	
56/62	WDR62
49/70	ATG7
49/55	RABGAP1
42/46	TBC1D2B
36/75	SQSTM1
36/36	USP28
34/90	ATG4B
21/196	GABARAPL2
19/19	MAP4K2
18/18	AKAP11
18/18	RABGAP1L
11/13	ATG3
8/8	RAB3GAP2
7/7	ATG13
7/7	RAB3GAP1
7/7	CFL1
2/2	ATG4C
Unique/Total	Prey

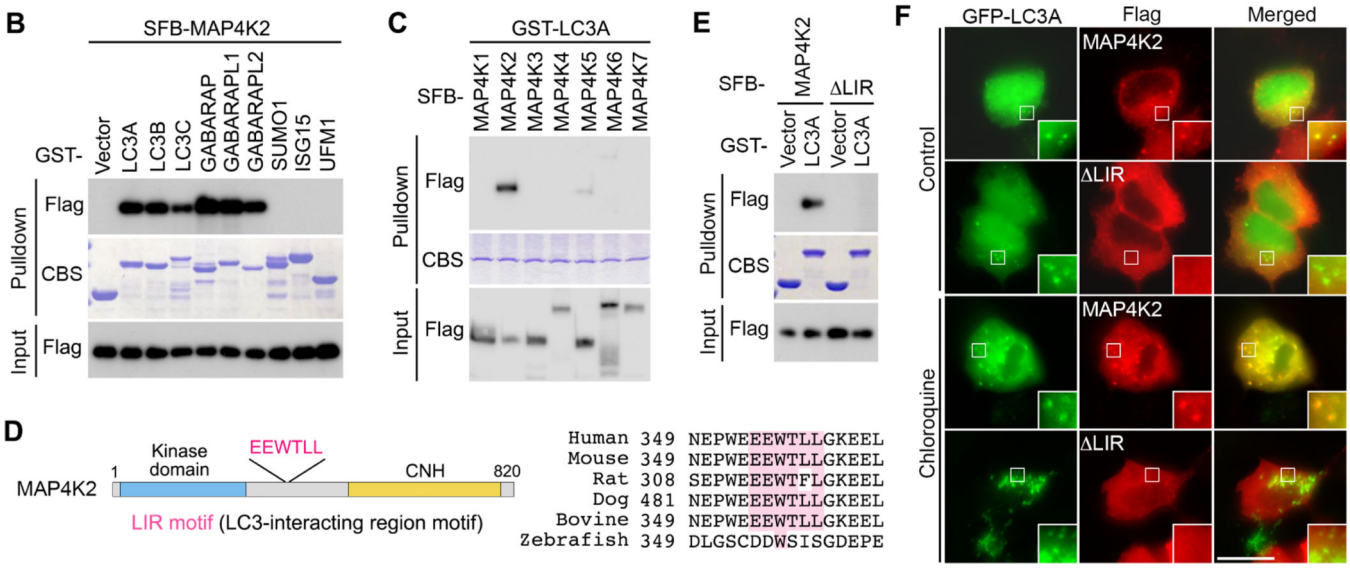

Figure 1. MAP4K2 binds ATG8 family of autophagy proteins.

(**A**) TAP-MS analysis reveals ATG8-family proteins as MAP4K2-binding proteins. The numbers of unique and total peptides for each identified protein are shown.

(**B**) Validation of the interaction between MAP4K2 and ATG8-family proteins. The indicated SFB-tagged constructs were expressed in HEK293T cells, incubated with the indicated bacterially purified GST-tagged proteins, and subjected to pulldown assay using glutathione agarose beads. CBS, Coomassie blue staining.

(**C**) LC3A strongly interacts with MAP4K2 among the MAP4K-family kinases.

(**D**) One LIR motif is identified in MAP4K2.

(**E**) The LIR motif is required for the interaction between MAP4K2 and LC3A. ΔLIR, MAP4K2 LIR deletion mutant.

(**F**) The LIR motif is required for the localization of MAP4K2 onto LC3A puncta. The constructs encoding SFB-tagged MAP4K2 and GFP-tagged LC3A were co-expressed in HEK293A cells, treated with DMSO or chloroquine (200 μM) for 2 hours, and subjected to

immunofluorescent staining. The indicated regions in the box are shown 3 times enlarged. Scale bar, 20 μm.

See also Figure S1 and Table S1.

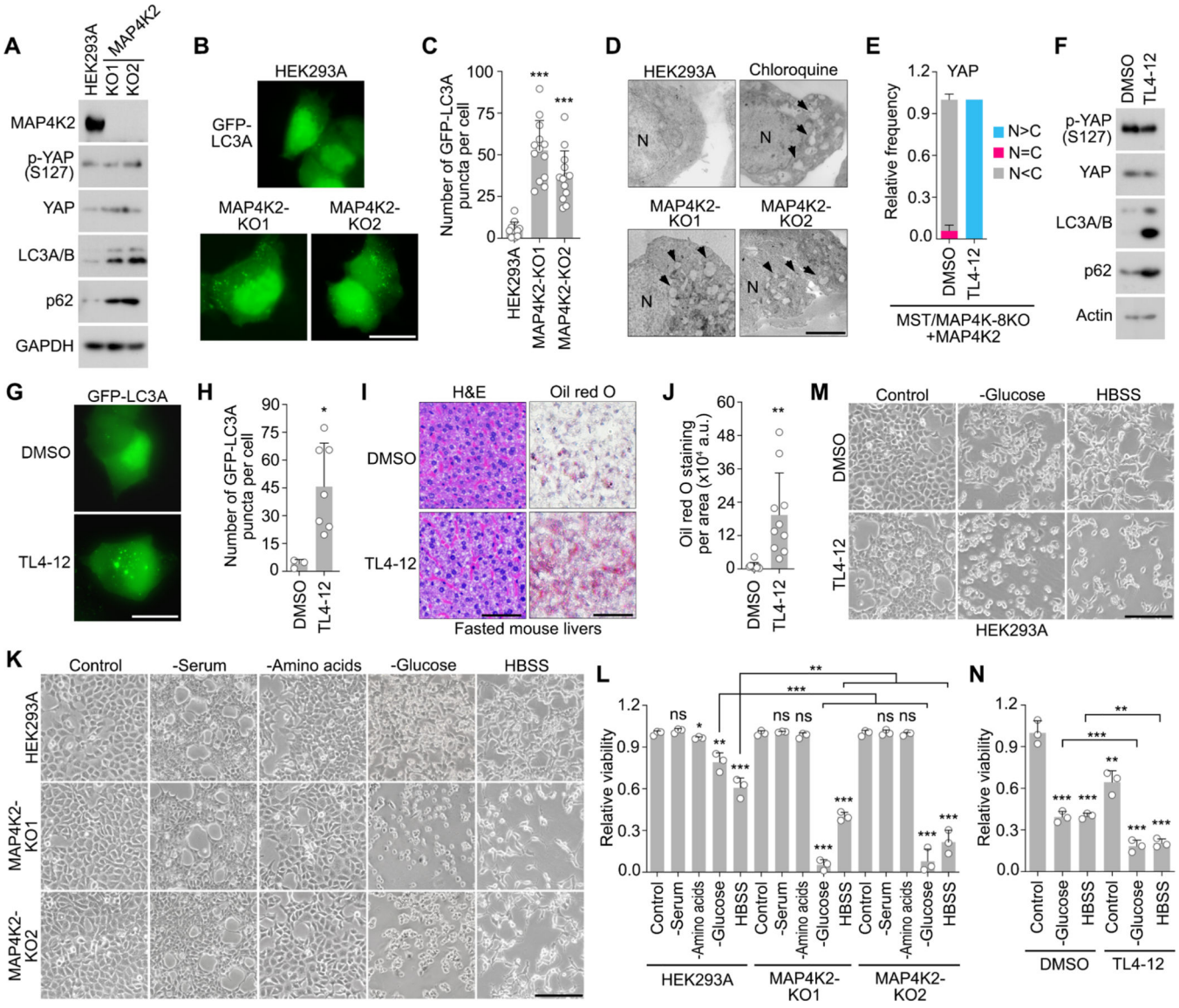

Figure 2. MAP4K2 is required for autophagy and cell survival under energy stress.

(**A**) Validation of the MAP4K2 knockout (KO) cells. Western blot was performed using the indicated antibodies. Cells were cultured in normal media.

(**B-C**) Loss of MAP4K2 increases GFP-LC3A puncta. The construct encoding GFP-LC3A was expressed in the indicated cells (**B**). The number of GFP-LC3A puncta was quantified (mean ± s.d.) (**C**). *** $p < 0.001$ (Student's *t*-test). Scale bar, 20 μm. Cells were cultured in normal media.

(**D**) MAP4K2 KO cells show accumulated vesicle-like structures. Transmission electron microscopy (TEM) analysis was performed for the indicated cells. Arrows indicate the accumulated vesicle-like structures. Cells were treated with chloroquine (200 μM) for 2 hours. N, nucleus. Scale bar, 4 μm.

(**E**) Validation of TL4-12 in targeting MAP4K2 activity. The MST/MAP4K-8KO cells were reconstituted with SFB-tagged MAP4K2, treated with DMSO or TL4-12 (20 μM) for 24 hours, and subjected to immunofluorescent staining using YAP antibody. Around 200 cells

in total were randomly selected and quantified for the YAP subcellular localization based on the average fluorescence intensity for YAP between nucleus (N) and cytoplasm (C) in each cell (mean ± s.d.).

(**F**) TL4-12 treatment increases LC3 and p62 expression. HEK293A cells were treated with DMSO or TL4-12 (20 μM) for 24 hours.

(**G-H**) TL4-12 treatment increases GFP-LC3A puncta. HEK293A cells were transfected with GFP-LC3A construct and treated with DMSO or TL4–12 (20 μM) for 24 hours (**G**). The number of GFP-LC3A puncta was quantified (mean ± s.d.) (**H**). * $p < 0.05$ (Student's *t*-test). Scale bar, 20 μm.

(**I-J**) TL4-12 treatment induces lipid droplet accumulation in the livers of fasted mice. Mice were intraperitoneally injected with vehicle control or TL4-12 (15 mg/kg) once a day for a week and fasted for 16 hours. Mouse livers were collected for hematoxylin and eosin (H&E) staining and oil red O staining (**I**). The oil red O staining of mouse liver tissues was quantified (mean ± s.d.)

(**H**). ** $p < 0.01$ (Student's *t*-test). Scale bar, 50 μm.

(**K-L**) Loss of MAP4K2 reduces cell viability under energy stress. Cells were subjected to the indicated stress conditions for 20 hours (**K**) and quantified for the relative viability (mean ± s.d., n=3 biological replicates) (**L**). ns, no significance. * $p < 0.05$, ** $p < 0.01$, *** $p < 0.001$ (Student's *t*-test). Scale bar, 200 μm.

(**M-N**) TL4-12 treatment reduces cell viability under energy stress. HEK293A cells were treated with DMSO control or TL4-12 (20 μM) and the indicated stress conditions for 20 hours (**M**) and quantified for the relative viability (mean ± s.d., n=3 biological replicates) (**N**). ** $p < 0.01$, *** $p < 0.001$ (Student's *t*-test). Scale bar, 200 μm.

See also Figure S2.

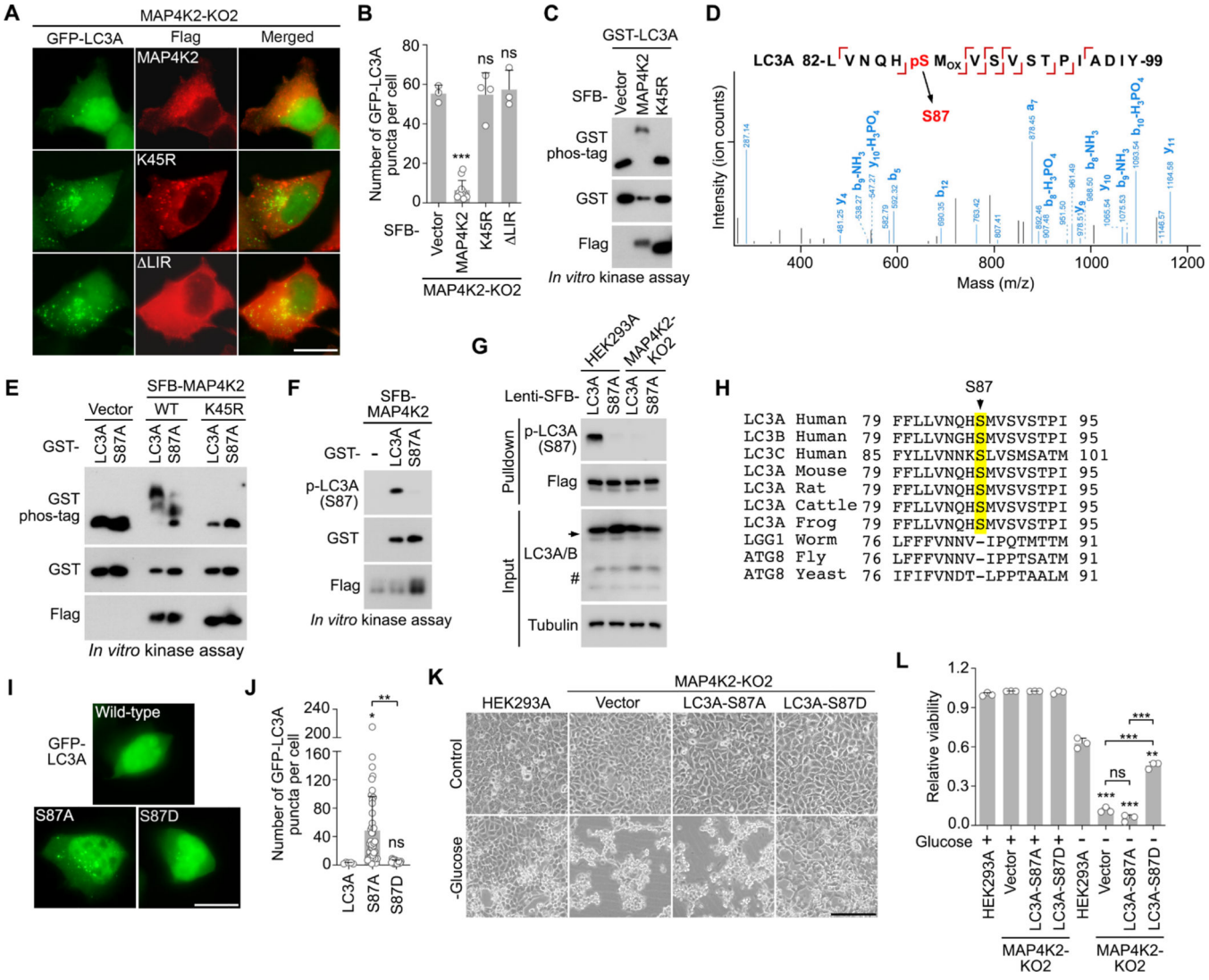

Figure 3. MAP4K2 promotes autophagy and cell survival by phosphorylating LC3A at S87.

(**A-B**) Both kinase activity and LIR motif are required for MAP4K2-mediated autophagy. The MAP4K2 KO cells were transfected with the indicated constructs and subjected to immunofluorescent staining (**A**). The number of GFP-LC3A puncta was quantified (mean ± s.d.) (**B**). ns, no significance. *** $p < 0.001$ (Student's *t*-test). Scale bar, 20 μm.

(**C**) MAP4K2 phosphorylates LC3A. SFB-tagged MAP4K2 and its kinase dead mutant (K45R) were expressed in HEK293T cells, purified using S protein beads, washed thoroughly with high-salt buffer containing 250 mM NaCl, and subjected to *in vitro* kinase assay using the bacterially purified GST-LC3A protein as substrate.

(**D**) Mass spectrometry reveals S87 as the MAP4K2 phosphorylation site on LC3A. GST-tagged LC3A protein was purified from bacteria, used as substrate in the SFB-MAP4K2 *in vitro* kinase assay, and subjected to mass spectrometry analysis.

(**E-G**) MAP4K2 phosphorylates LC3A at S87. *In vitro* kinase assay was performed using the indicated bacterially purified GST-tagged proteins as substrates (**E**). MAP4K2-induced LC3A phosphorylation at S87 was validated using anti-phospho-LC3A S87 antibody via *in*

vitro kinase assay (**F**). Wild-type and the MAP4K2 KO HEK293A cells were transduced with the inducible lenti-SFB-LC3A and its S87A mutant, treated with doxycycline at low concentration, and purified using S protein beads (**G**). Arrow indicates the exogenously expressed SFB-LC3A and its S87A mutant. Pound sign indicates endogenous LC3A/B.
(**H**) Protein sequence alignment shows that LC3A S87 site is conserved among all the LC3 proteins in mammals and amphibians.
(**I**-**J**) The S87A mutation increases LC3A puncta. HEK293A cells were transfected with the constructs encoding the indicated GFP-tagged LC3A and its mutants (**I**). The number of GFP-LC3A puncta was quantified (mean ± s.d.) (**J**). ns, no significance. * $p < 0.05$, ** $p < 0.01$ (Student's *t*-test). Scale bar, 20 μm. Cells were cultured in normal media.
(**K**-**L**) Reconstituting LC3A S87D mutant but not its S87A mutant rescues MAP4K2 KO cell viability under glucose starvation. The MAP4K2 KO cells were transduced with the indicated constructs and subjected to glucose starvation for 20 hours (**K**). Relative cell viability was quantified (mean ± s.d.) (**L**). ns, no significance. ** $p < 0.01$, *** $p < 0.001$ (Student's *t*-test). Scale bar, 200 μm.
See also Figure S3.

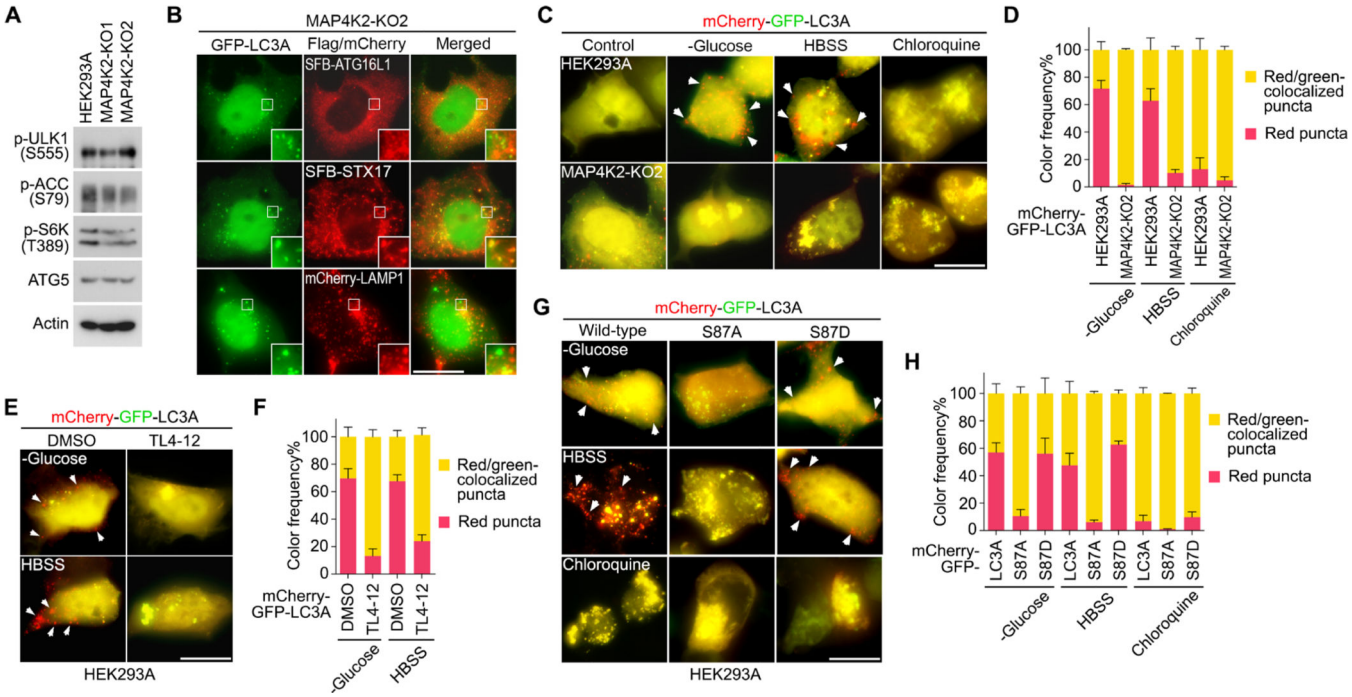

Figure 4. MAP4K2-mediated LC3A S87 phosphorylation facilitates autophagosome-lysosome fusion.

(**A**) Loss of MAP4K2 does not affect the key components/regulators of autophagy.

(**B**) GFP-LC3A puncta are accumulated at late autophagosome stage in the MAP4K2 KO cells. The indicated regions in the box are shown 3 times enlarged. Scale bar, 20 μm. Cells were cultured in normal media.

(**C-D**) Loss of MAP4K2 inhibits autophagosome-lysosome fusion. Wild-type and the MAP4K2 KO HEK293A cells were transfected with mCherry-GFP-LC3A construct and treated with glucose starvation and HBSS for 16 hours or chloroquine (200 μM) for 2 hours. Representative fluorescent images were shown (**C**). Around 50 cells in total were randomly selected and quantified for the yellow- and red-colored LC3A puncta (mean ± s.d.) (**D**). Arrows indicate the mCherry-GFP-LC3A puncta fused with lysosomes. Scale bar, 20 μm.

(**E-F**) TL4–12 treatment inhibits autophagosome-lysosome fusion. HEK293A cells were transfected with mCherry-GFP-LC3A construct and treated with DMSO or TL4–12 (20 μM) and glucose starvation and HBSS for 16 hours. Representative fluorescent images were shown (**E**). Around 50 cells in total were randomly selected and quantified for the yellow- and red-colored LC3A puncta (mean ± s.d.) (**F**). Arrows indicate the mCherry-GFP-LC3A puncta fused with lysosomes. Scale bar, 20 μm.

(**G-H**) LC3A S87 phosphorylation is required for autophagosome-lysosome fusion. HEK293A cells were transfected with mCherry-GFP-LC3A and its S87A and S87D mutants and treated with glucose starvation and HBSS for 16 hours or chloroquine (200 μM) for 2 hours.

Representative fluorescent images were shown (**G**). Around 50 cells in total were randomly selected and quantified for the yellow- and red-colored puncta of LC3A and its S87A and S87D mutants (mean ± s.d.) (**H**). Arrows indicate the mCherry-GFP-LC3A and its mutant puncta fused with lysosomes. Scale bar, 20 μm.

See also Figures S3 and S4.

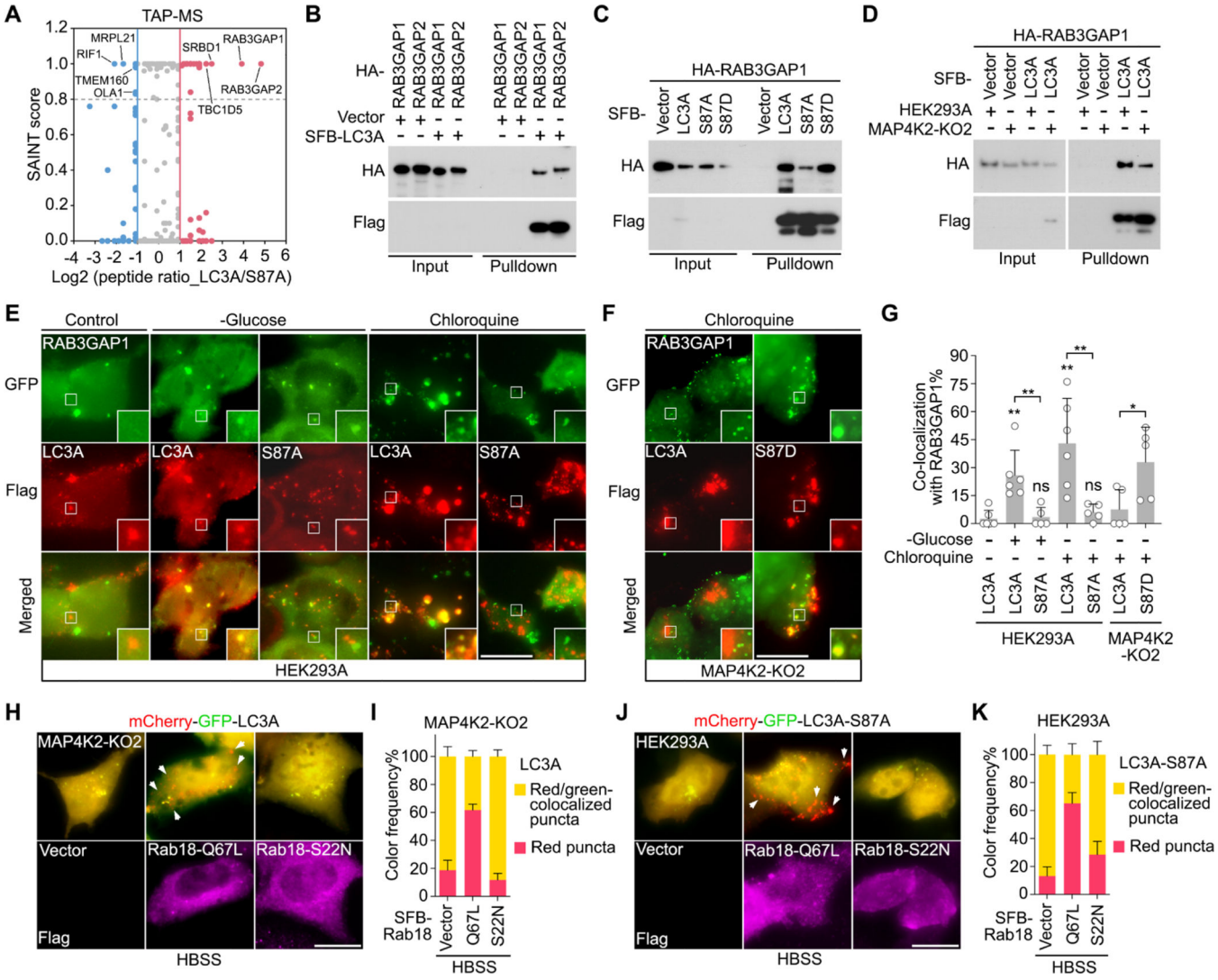

Figure 5. LC3A S87 phosphorylation drives autophagosome-lysosome fusion through the RAB3GAP1/2-Rab18 pathway.

(**A**) Comparative proteomic analysis reveals RAB3GAP1/2 as LC3A-binding proteins regulated by its S87 phosphorylation. HEK293A cells stably expressing LC3A and its S87A mutant were cultured under glucose starvation for 16 hours and subjected to the TAP-MS analysis. The identified interacting proteins were visualized as the volcano plot based on the ratio of their normalized peptide numbers (LC3A versus its S87A mutant) and SAINT scores. Preys with SAINT score ≥ 0.8 (either LC3A or its S87A mutant TAP-MS study) and peptide ratio over two times (either <0.5 or >2) were gated for analysis. The representative LC3A-interacting proteins regulated by LC3A S87 phosphorylation were indicated.

(**B**) LC3A interacts with RAB3GAP1/2.

(**C**) The S87A mutation inhibits the association of LC3A with RAB3GAP1.

(**D**) Loss of MAP4K2 attenuates the interaction between LC3A and RAB3GAP1.

(**E**) RAB3GAP1 is co-localized with LC3A but not its S87A mutant under glucose starvation and chloroquine treatment. HEK293A cells were transfected with the indicated constructs, treated with glucose starvation for 16 hours or chloroquine (200 μM) for 2 hours,

and subjected to immunofluorescent staining. The indicated regions in the box are shown 3 times enlarged. Scale bar, 20 μm.

(**F**) RAB3GAP1 is co-localized with LC3A S87D mutant in the chloroquine-treated MAP4K2 KO cells. The MAP4K2 KO cells were transfected with the indicated constructs, treated with chloroquine (200 μM) for 2 hours, and subjected to immunofluorescent staining. The indicated regions in the box are shown 3 times enlarged. Scale bar, 20 μm.

(**G**) The co-localization of RAB3GAP1 with the indicated LC3A and its mutants in (**E**) and (**F**) was quantified (mean ± s.d.). ns, no significance. * $p < 0.05$, ** $p < 0.01$, *** $p < 0.001$ (Student's *t*-test).

(**H-K**) LC3A S87 phosphorylation drives autophagosome-lysosome fusion through Rab18. The mCherry-GFP-LC3A-indicated autophagosome-lysosome fusion in the HBSS-treated MAP4K2 KO cells was rescued by expressing Rab18 constitutively active mutant (Q67L) but not its inactive mutant (S22N) (**H**) and quantified (**I**). The mCherry-GFP-LC3A S87A-indicated autophagosome-lysosome fusion defect in the HBSS-treated HEK293A cells was rescued by expressing Rab18 constitutively active mutant (Q67L) but not its inactive mutant (S22N) (**J**) and quantified (**K**). Arrows indicate the mCherry-GFP-LC3A or its S87A mutant puncta fused with lysosomes. Scale bar, 20 μm.

See also Figures S4.

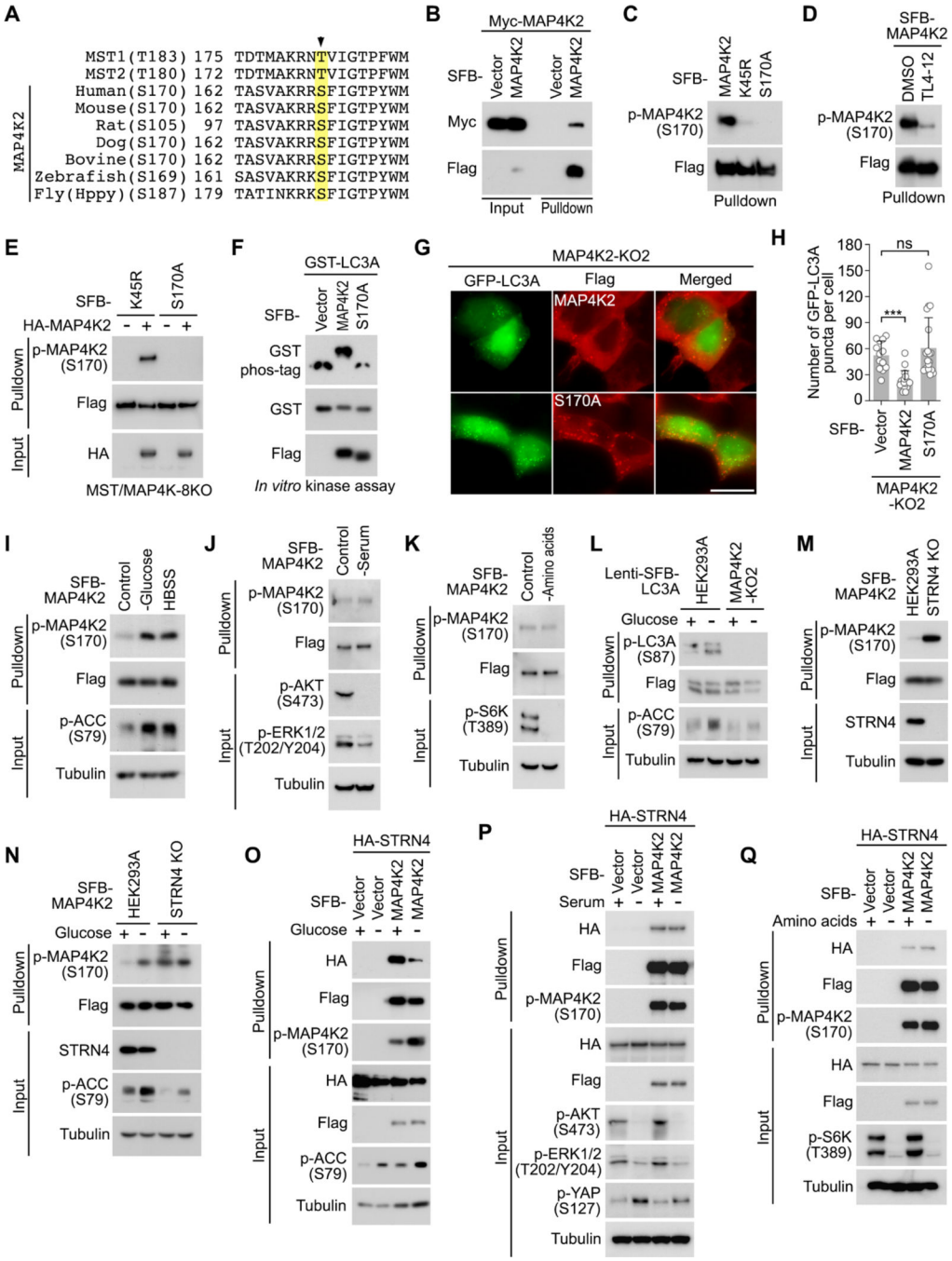

Figure 6. Energy stress activates MAP4K2 by inhibiting its association with the STRIPAK^{STRN4} complex.

(**A**) Protein sequence alignment reveals S170 as a potential autophosphorylation site of MAP4K2.

(**B**) MAP4K2 binds itself.

(**C-D**) MAP4K2 kinase activity is required for its S170 phosphorylation. MAP4K2 S170 phosphorylation was largely reduced in its kinase dead mutant (K45R) (**C**) or in the TL4-12-treated cells (**D**). Cells were treated with TL4-12 (20 μM) for 24 hours.

(**E**) MAP4K2 induces S170 phosphorylation of its K45R mutant in the MST/MAP4K-8KO HEK293A cells.

(**F-H**) The S170A mutation inhibits MAP4K2. *In vitro* kinase assay was performed using the bacterially purified GST-LC3A protein as substrate (**F**). The MAP4K2 KO HEK293A cells were reconstituted with the indicated constructs and subjected to immunofluorescent staining (**G**). The number of GFP-LC3A puncta was quantified (mean ± s.d.) (**H**). ns, no significance. *** $p < 0.001$ (Student's *t*-test). Scale bar, 20 μm. Cells were cultured in normal media.

(**I-K**) Energy stress induces MAP4K2 S170 phosphorylation. HEK293A cells were transfected with the construct encoding SFB-MAP4K2, treated with glucose starvation (**I**), HBSS (**I**), serum starvation (**J**) or amino acids starvation (**K**) for 16 hours, and subjected to pulldown assay using S protein beads.

(**L**) Glucose starvation induces LC3A S87 phosphorylation. Wild-type and the MAP4K2 KO HEK293A cells were transduced with inducible lentiviral SFB-LC3A, treated with doxycycline at low concentration and glucose starvation for 16 hours, and subjected to pulldown assay using S protein beads.

(**M**) Loss of STRN4 increases MAP4K2 S170 phosphorylation.

(**N**) Glucose starvation does not further increase MAP4K2 S170 phosphorylation in the STRN4 KO cells. Wild-type and the STRN4 KO HEK293A cells were transfected with SFB-MAP4K2 construct, treated with glucose starvation for 16 hours, and subjected to pulldown assay using S protein beads.

(**O-Q**) Glucose starvation inhibits the interaction between MAP4K2 and STRN4. HEK293A cells were transfected with the indicated constructs, treated with glucose starvation (**O**), serum starvation (**P**) or amino acids starvation (**Q**) for 16 hours, and subjected to pulldown assay using S protein beads.

See also Figures S5.

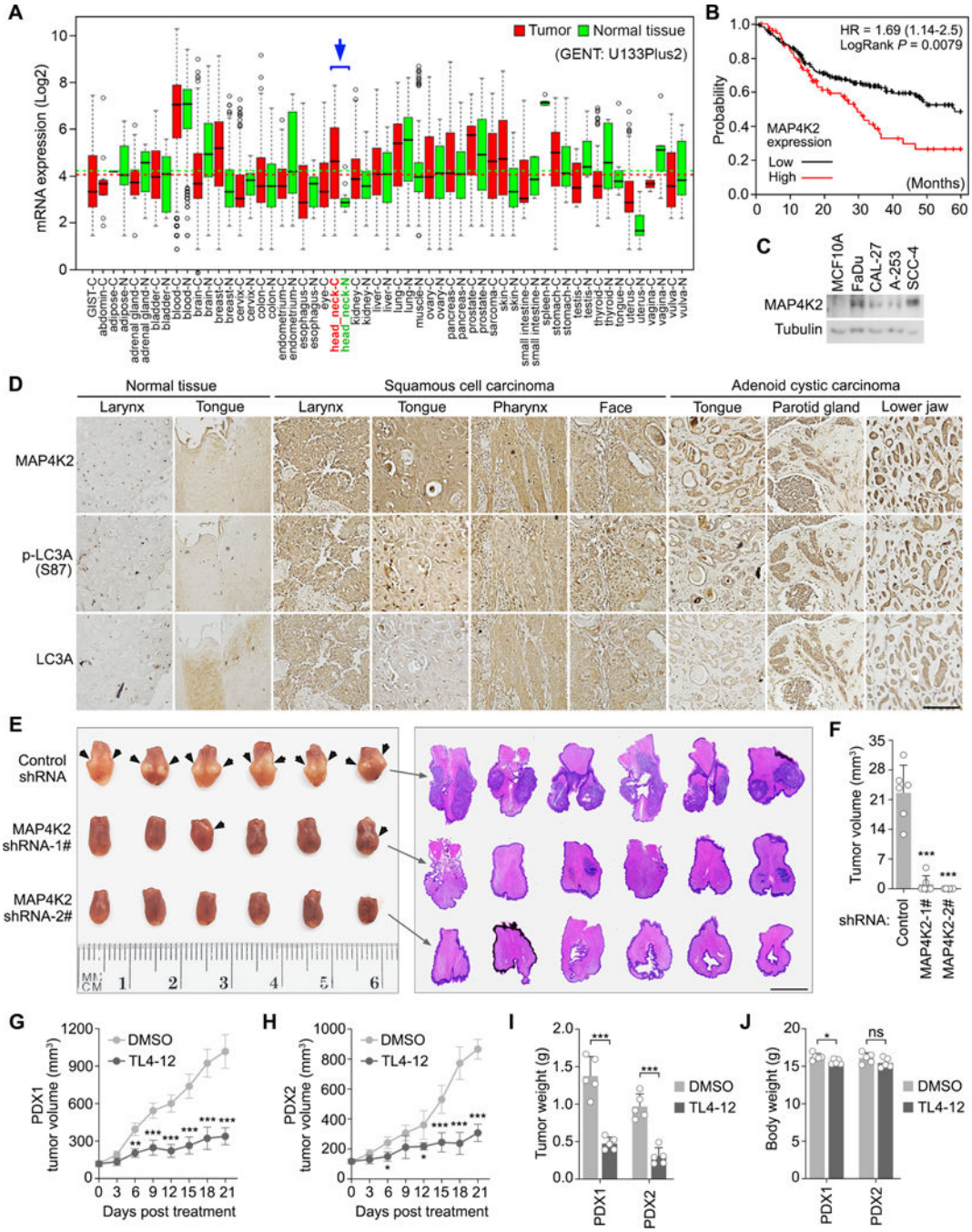

Figure 7. MAP4K2 acts as an oncoprotein in head and neck cancer.

(**A**) mRNA level of *MAP4K2* is compared between tumor and normal tissues across different types of human cancer using the Gene Expression database of Normal and Tumor tissues (GENT), where more than 40,000 tumor sample data are included. The first quartile, median and third quartile values were indicated as the boxplots. Outliers were plotted as individual points. Error bars indicated the standard deviation above and below the mean of the data.

(**B**) Kaplan-Meier curves of overall survival of patients with head and neck squamous cell carcinoma is stratified by *MAP4K2* expression level. Clinical data of *MAP4K2* were analyzed in Kaplan-Meier Plotter Pan-cancer RNA-seq project (https://kmplot.com/analysis/) containing a total of 500 head and neck cancer patient samples with high mutation burden. The *p* value was calculated by using the log-rank (Mantel-Cox) test.
(**C**) MAP4K2 is highly expressed in head and neck cancer cells.
(**D**) Head and neck cancer tissue microarray is subjected to immunohistochemistry analysis using the indicated antibodies. Scale bar, 150 μm.
(**E-F**) Downregulation of MAP4K2 inhibits CAL-27 xenograft tumor growth in mouse tongues. MAP4K2 shRNA-transduced CAL-27 cells were subjected to the orthotopic xenograft study, where the collected mouse tongues and their hematoxylin and eosin (H&E) staining were shown
(**E**). Tumors are indicated with arrows. Tumor volume was measured and quantified (mean ± s.d., n=6 mice per group) (**F**). *** $p < 0.001$ (Student's *t*-test). Scale bar, 3 mm.
(**G-J**) Tumors developed from two patients with tongue squamous carcinoma were implanted into mice and subjected to TL4–12 treatment (15 mg/kg). PDX tumor size was measured every 3 days using a caliper (**G-H**), while the tumor weight (**I**) and mouse body weight (**J**) were measured at the endpoint (mean ± s.d., n=5 mice per group). ns, no significance. * $p < 0.05$, ** $p < 0.01$, *** $p < 0.001$ (Student's *t*-test). See also Figures S6 and S7.

Key resources table

REAGENT or RESOURCE	SOURCE	IDENTIFIER
Antibodies		
Anti-Flag	Sigma-Aldrich	Cat# F7425, RRID:AB_439687
Anti-Flag (M2)	Sigma-Aldrich	Cat# F3165, RRID:AB_259529
Anti-thiophosphate ester	Abcam	Cat# ab92570, RRID:AB_10562142
Anti-STRN4	Bethyl lab	Cat# A304-573A-M, RRID:AB_2782004
Anti-STRIP1	Bethyl lab	Cat# A304-644A, RRID:AB_2620839
Anti-LC3A/B	Cell Signaling Technology	Cat# 12741, RRID:AB_2617131
Anti-p62	Cell Signaling Technology	Cat# 88588, RRID:AB_2800125
Anti-GAPDH	Cell Signaling Technology	Cat# 5174, RRID:AB_10622025
Anti-LC3A	Cell Signaling Technology	Cat# 4599, RRID:AB_10548192
Anti-phospho-ULK1 (S555)	Cell Signaling Technology	Cat# 5869, RRID:AB_10707365
Anti-phospho-ACC (S79)	Cell Signaling Technology	Cat# 3661, RRID:AB_330337
Anti-phospho-S6K (T389)	Cell Signaling Technology	Cat# 9234, RRID:AB_2269803
Anti-phospho-AKT (S473)	Cell Signaling Technology	Cat# 4060, RRID:AB_2315049
Anti-phospho-ERK1/2 (T202/Y204)	Cell Signaling Technology	Cat# 4370, RRID:AB_2315112
Anti-PP2A C	Cell Signaling Technology	Cat# 2038, RRID:AB_2169495
Anti-LATS1	Cell Signaling Technology	Cat# 3477, RRID:AB_2133513
Anti-phospho-LATS1 (T1079)	Cell Signaling Technology	Cat# 8654, RRID:AB_10971635
Anti-phospho-YAP (S127)	Cell Signaling Technology	Cat# 4911, RRID:AB_2218913
Anti-hemagglutinin (HA)	BioLegend	Cat# MMS-101P, RRID:AB_2314672
Anti-phospho-MAP4K2 (S170)	Kinexus	Cat# AB-PK646, RRID:AB_2938947
Anti-YAP	Santa Cruz Biotechnology	Cat# sc-101199, RRID:AB_1131430
Anti-Myc	Santa Cruz Biotechnology	Cat# sc-40, RRID:AB_627268
Anti-SLMAP	Santa Cruz Biotechnology	Cat# sc-100957, RRID:AB_2286621
Anti-MOB4	Santa Cruz Biotechnology	Cat# sc-137228, RRID:AB_2145393
Anti-Flag (M2)	Sigma-Aldrich	Cat# F3165, RRID:AB_259529
Anti-α-tubulin	Sigma-Aldrich	Cat# T6199, RRID:AB_477583
Anti-β-actin	Sigma-Aldrich	Cat# A5441, RRID:AB_476744
Anti-STRN	Thermo Fisher Scientific	Cat# A304-537A-M, RRID:AB_2781976
Anti-STRN3	Thermo Fisher Scientific	Cat# PA5-31368, RRID:AB_2548842
Anti-GST	This paper	N/A
Anti-MAP4K2	This paper	N/A
Anti-phospho-LC3A (S87)	This paper	N/A
Anti-MBP	This paper	N/A
Anti-CTTNBP2NL	This paper	N/A
Anti-YAP	Wang et al. 2011[68]	N/A
Bacterial and virus strains		

REAGENT or RESOURCE	SOURCE	IDENTIFIER
DH5α competent *E. coli*	Junjie Chen laboratory	N/A
BL21 competent *E. coli*	Junjie Chen laboratory	N/A
DB3.1 competent *E. coli*	Junjie Chen laboratory	N/A
Biological samples		
Head and neck cancer tissue arrays	US Biomax, Inc	Cat# HN242b, Cat# HN802c
Chemicals, peptides, and recombinant proteins		
Hexadimethrine bromide (Polybrene)	Sigma-Aldrich	Cat# H9268
Streptavidin-conjugated bead	GE Healthcare	Cat# 17-5113-01
Chloroquine	MP Biomedicals	Cat# 193919
Phos-tag Acrylamide	FUJIFILM Wako Chemicals	Cat# AAL-107
S protein bead	Novagen	Cat# 69704
3-Methyladenine	Selleckchem	Cat# S2767
4′,6-diamidino-2-phenylindole (DAPI)	Sigma-Aldrich	Cat# D9542
Chymotrypsin, Sequencing Grade	Promega	Cat# V106A
Biotin	Sigma-Aldrich	Cat# B4639
TRIzol	Thermo Fisher	Cat# 15596026
Power SYBR Green PCR master mix	Thermo Fisher	Cat# 4367659
TL4-12	TOCRIS	Cat# 5910
MBP-LATS1-C3 (981~1130 amino acids)	Han et al., 2018[24]	N/A
GST-LC3A	This paper	N/A
GST-LC3B	This paper	N/A
GST-LC3C	This paper	N/A
GST-GABARAP	This paper	N/A
GST-GABARAPL1	This paper	N/A
GST-GABARAPL2	This paper	N/A
GST-SUMO1	This paper	N/A
GST-ISG15	This paper	N/A
GST-UFM1	This paper	N/A
GST-LC3A S87A	This paper	N/A
GST-LC3B S87A	This paper	N/A
GST-LC3C S93A	This paper	N/A
GST-GABARAP T87A	This paper	N/A
GST-LC3A S87A+S3A	This paper	N/A
GST-LC3A S87A+S12A	This paper	N/A
GST-LC3A S87A+S29A	This paper	N/A
GST-LC3A S87A+T50A	This paper	N/A
GST-LC3A S87A+S61A	This paper	N/A
GST-LC3A S87A+T76A	This paper	N/A
GST-LC3A S87A+S90A	This paper	N/A

REAGENT or RESOURCE	SOURCE	IDENTIFIER
GST-LC3A S87A+S92A	This paper	N/A
GST-LC3A S87A+T93A	This paper	N/A
GST-LC3A S87A+S115A	This paper	N/A
GST-LC3A S87A+T118A	This paper	N/A
GST-LC3A S87A+S115/T118A	This paper	N/A
GST-LC3A S87A+S12A/S115A	This paper	N/A
GST-LC3A S87A+S12A/T118A	This paper	N/A
Critical commercial assays		
Gateway BP Clonase Enzyme Mix for BP assay	Thermo Fisher	Cat# 11789021
Gateway LR Clonase Enzyme Mix for LR assay	Thermo Fisher	Cat# 11791043
Script Reverse Transcription Supermix Kit for reverse transcription assay	BioRad	Cat# 1708841
Deposited data		
Unprocessed imaging data	This paper/Mendeley Data	DOI:10.17632/dxzjr2z5yz.2
Experimental models: Cell lines		
HEK293T	ATCC	Cat# CRL-2316
HEK293A	Jae-Il Park laboratory/Thermo Fisher Scientific	Cat# R70507
CAL-27	ATCC	Cat# CRL-2095
FaDu	ATCC	Cat# HTB-43
A253	ATCC	Cat# HTB-41
SCC-4	ATCC	Cat# CRL-1624
MCF10A	ATCC	Cat# CRL-10317
BxPC3	ATCC	Cat# CRL-1687
PANC1	ATCC	Cat# CRL-1469
Hep3B	ATCC	Cat# HB-8064
HepG2	ATCC	Cat# HB-8065
MDA-MB-231	ATCC	Cat# CRM-HTB-26
HeLa	Junjie Chen laboratory/ATCC	Cat# CRM-CCL-2
Experimental models: Organisms/strains		
C57BL/6J mouse	Jackson Laboratory	Cat# 000664; RRID:IMSR_JAX:000664
Athymic nude (nu/nu) mouse	Jackson Laboratory	Cat# 002019; RRID:IMSR_JAX:002019
NOD-SCID-IL2rg (NSG) mice	Biocytogen Pharmaceuticals (Beijing) Co., Ltd.	N/A
Oligonucleotides		
MAP4K2 sgRNAs	This paper	Table S2
MAP4K2 shRNAs	This paper	Table S2
Recombinant DNA		
Lenti Guide-Puro	Addgene	Cat# 52963
Lenti Cas9-Blast	Addgene	Cat# 52962
pDEST-CMV-N-Tandem-mCherry-EGFP	Addgene	Cat# 123216

REAGENT or RESOURCE	SOURCE	IDENTIFIER
HA-p62	Addgene	Cat# 28027
pME18s-HA-FIP200	Addgene	Cat# 243033
pBMN PLEKHM1-HA	Addgene	Cat# 89300
PLKO.1 control shRNA	Addgene	Cat# 136035
MAP4K2 shRNA-1#	Sigma-Aldrich	#TRCN0000195052
MAP4K2 shRNA-2#	Sigma-Aldrich	#TRCN0000199054
HA-NBR1	This paper	N/A
HA-FYCO1	This paper	N/A
GFP-LC3A	This paper	N/A
GFP-LC3A S87A	This paper	N/A
GFP-LC3A S87D	This paper	N/A
GFP-LC3B	This paper	N/A
GFP-LC3B S87A	This paper	N/A
GFP-LC3C	This paper	N/A
GFP-LC3C S93A	This paper	N/A
GFP-RAB3GAP1	This paper	N/A
HA-LC3A	This paper	N/A
HA-LC3A S87A	This paper	N/A
HA-LC3A S87D	This paper	N/A
HA-NDP52	This paper	N/A
HA-RAB3GAP1	This paper	N/A
HA-RAB3GAP2	This paper	N/A
HA-STRN4	This paper	N/A
Lenti-RAB18 Q67L-SFB	This paper	N/A
Lenti-RAB18 S22N-SFB	This paper	N/A
Lenti-SFB-LC3A	This paper	N/A
Lenti-SFB-LC3A S87A	This paper	N/A
mCherry-GFP-LC3A	This paper	N/A
mCherry-GFP-LC3A S87A	This paper	N/A
mCherry-GFP-LC3A S87D	This paper	N/A
mCherry-GFP-LC3B	This paper	N/A
mCherry-GFP-LC3B S87A	This paper	N/A
mCherry-GFP-LC3C	This paper	N/A
mCherry-GFP-LC3C S93A	This paper	N/A
mCherry-LAMP1	This paper	N/A
Myc-MAP4K2	This paper	N/A
SFB-ATG16L1	This paper	N/A
SFB-LC3A	This paper	N/A
SFB-LC3A S87A	This paper	N/A

REAGENT or RESOURCE	SOURCE	IDENTIFIER
SFB-LC3A S87D	This paper	N/A
SFB-MAP4K1	Seo et al., 2020[11]	N/A
SFB-MAP4K2	Seo et al., 2020[11]	N/A
SFB-MAP4K2 ΔLIR	This paper	N/A
SFB-MAP4K2 K45R	This paper	N/A
SFB-MAP4K2 S170A	This paper	N/A
SFB-MAP4K3	Seo et al., 2020[11]	N/A
SFB-MAP4K4	Seo et al., 2020[11]	N/A
SFB-MAP4K5	Seo et al., 2020[11]	N/A
SFB-MAP4K6	Seo et al., 2020[11]	N/A
SFB-MAP4K7	Seo et al., 2020[11]	N/A
SFB-PLEKHM1	This paper	N/A
SFB-RAB18 Q67L	This paper	N/A
SFB-RAB18 S22N	This paper	N/A
SFB-STX17	This paper	N/A
Software and algorithms		
Optimized CRISPR Design	CHOPCHOP	http://chopchop.cbu.uib.no/
ImageJ	ImageJ	RRID: SCR_003070
Metascape	Metascape	www.metascape.org
GraphPad Prism 6	GraphPad	RRID:SCR_002798
BioRENDER	BioRENDER	http://biorender.com
Other		
DMEM (1X) [-] D-Glucose [-] Sodium pyruvate	Gibco	Cat# 11966025
HBSS (1X)	Gibco	Cat# 14025076
DMEM without amino acids	Thermo Fisher Scientific	https://www.thermofisher.com/us/en/home/technical-resources/media-formulation.8.html (amino acids are not added)